Title: Longitudinal immune dynamics of mild COVID-19 define signatures of recovery and persistence

Authors:

Aarthi Talla[1*], Suhas V. Vasaikar[1*], Maria P. Lemos[2$], Zoe Moodie[2$], Mark-Phillip Lee Pebworth[1%], Kathy E. Henderson[1%], Kristen W. Cohen[2%], Julie L. Czartoski[2%], Lilin Lai[3,4], Mehul S. Suthar[3,4], Alexander T Heubeck[1], Palak C. Genge[1], Charles R. Roll[1], Morgan Weiss[1], Julian Reading[1], Nina Kondza[1], Hugh MacMillan[2], Olivia C. Fong[1], Zachary James Thomson[1], Lucas T. Graybuck[1], Evan W. Newell[2], Ernest M. Coffey[1], Paul Meijer[1], Lynne A. Becker[1], Stephen C. De Rosa[2], Troy R. Torgerson[1], Peter J. Skene[1], Xiaojun Li[1], Gregory Lee Szeto[1#], M. Juliana McElrath[2#], Thomas F. Bumol[1#]

Affiliations:

[1]Allen Institute for Immunology, Seattle, WA 98109, USA
[2]Vaccine and Infectious Disease Division, Fred Hutchinson Cancer Research Center, Seattle, WA 98109, USA
[3]Center for Childhood Infections and Vaccines of Children's Healthcare of Atlanta, Emory University Department of Pediatrics Department of Medicine, Atlanta, GA 30322 USA
[4]Yerkes National Primate Research Center, Atlanta, GA 30329, USA

* These authors contributed equally to this work.
$ These authors contributed equally to this work.
% These authors contributed equally to this work.
# Address correspondence to: Greg Szeto (greg.szeto@alleninstitute.org), M. Juliana McElrath (jmcelrat@fredhutch.org), and Thomas F. Bumol (tomb@alleninstitute.org)

Summary:

SARS-CoV-2 has infected over 160 million and caused more than 3 million deaths to date. Most individuals (>80%) have mild symptoms and recover in the outpatient setting, but detailed studies of immune responses have focused primarily on moderate to severe COVID-19. We deeply profiled the longitudinal immune response in individuals with mild COVID beginning with early time points post-infection (1-15 days) and proceeding through convalescence to >100 days after symptom onset. We correlated data from single cell analyses of peripheral blood cells, serum proteomics, virus-specific cellular and humoral immune responses, and clinical metadata. Acute infection was characterized by vigorous coordinated innate and adaptive activation, including an early cellular and proteomic signature that correlated with the amplitude of virus-specific humoral responses after day 30. We characterized signals associated with recovery and convalescence to define a new signature of inflammatory cytokines, gene expression, and chromatin accessibility that persists in individuals with post-acute sequelae of SARS-CoV-2 infection (PASC).

Keywords:

scRNAseq - single-cell ribonucleic acid sequencing
scATACseq - single-cell assay for transposase-accessible chromatin
PASC - post-acute sequelae SARS-CoV-2 infection
PSO - Post-Symptom Onset
RBD - Receptor Binding Domain

Introduction:

Severe acute respiratory syndrome-related coronavirus (SARS-CoV-2) is a novel, highly infectious human betacoronavirus that was first detected in late 2019, and has precipitated an ongoing pandemic that has infected >160 million people and killed over 3 million worldwide (Johns Hopkins COVID-19 dashboard, WHO dashboard). COVID-19, the clinical disease associated with SARS-CoV-2 infection, commonly presents with one or more respiratory symptoms, and may be accompanied by fatigue, fever, and often altered smell and taste; these can vary in severity with outcomes ranging from asymptomatic or mild to severe and fatal. There is substantial interindividual heterogeneity of severity, but more than 80% of infections are mild and individuals recover without hospitalization (Wu and McGoogan, 2020). Given the scale of worldwide infections, it is important to understand details of the normal, productive immune response to SARS-CoV-2 in mild COVID-19 infected individuals, who like those with more severe disease may experience persistent or recurrent symptoms. An estimated 30% to >70% of individuals with mild disease go on to develop post-acute sequelae of SARS-CoV2 infection (PASC or long COVID), an umbrella designation for clinical symptoms persisting weeks to months post-infection (Davis et al., 2020; Dennis et al.; Huang et al., 2021; Logue et al., 2021; Sudre et al., 2021).

The immune response to acute infection is critical to limit viral replication, activate innate immune cells, and efficiently prime virus-specific adaptive responses. Viral infections are rapidly sensed by pattern recognition receptors (PRRs) in infected cells and innate phagocytes, producing a key mediator of antiviral defense- interferons (IFNs). IFNs have delayed dynamics or are absent in severe COVID-19 (Galani et al., 2021; Hadjadj et al., 2020; Lucas et al., 2020) with multiple potential causes, including inefficient induction of type I and III IFNs in SARS-CoV-2-infected cells (Blanco-Melo et al., 2020), increased plasmacytoid dendritic cell (pDC) apoptosis and functional impairment (Arunachalam et al., 2020; Liu et al., 2021), and intrinsic type I IFN deficits such as somatic mutations or anti-IFN autoantibodies (Bastard et al., 2020; Wang et al., 2020; Zhang et al., 2020). Other hallmarks of acute infection in severe COVID-19 include lymphopenia, impaired early IFN-stimulated genes (ISG) expression in monocytes, and robust plasmablast expansion and extrafollicular B cell responses (Mathew et al., 2020; Schulte-Schrepping et al., 2020; Woodruff et al., 2020). It is unclear if any of these features are shared with mild COVID-19, whether they are correlated with each other, and how they impact clinical outcome and convalescent immunity in this subset of disease. Understanding immune mechanisms of a successful acute infection response in mild COVID-19 and how these correlate with SARS-CoV-2-specific adaptive immune responses is critical to identifying biomarkers and potential therapeutic strategies to limit disease severity in SARS-CoV-2 infection.

Efficient resolution of inflammatory responses is necessary for recovery from acute infection. Failure to coordinate the kinetics or magnitude of inflammation can lead to dysregulated innate, cellular, and humoral immune responses (Carvalho et al., 2021; Schultze and Aschenbrenner, 2021; Sette and Crotty, 2021). A persistent inflammatory state is a characteristic of children and adults with multisystem inflammatory syndrome (MIS-C and MIS-A), including elevated inflammatory cytokines and chemokines in blood with similarities to secondary hemophagocytic lymphohistiocytosis (HLH) and cytokine release syndrome (CRS) (Consiglio et al., 2020; Fajgenbaum and June, 2020; Morris et al., 2020; Shaigany et al., 2020; Vella et al., 2020). In contrast, a typical mild COVID-19 trajectory and degree of interindividual heterogeneity remains poorly characterized. Detailed analysis of longitudinal trajectories is needed to identify key events for successful resolution of acute infection, and points of coordination between innate and adaptive immune responses over time. Analysis of immune response kinetics can also determine if persistence of symptoms in PASC is characterized by unique trajectories, and whether inflammatory responses are prolonged compared to successful convalescent cases.

To further our understanding of mild COVID-19, we performed longitudinal, deep immune phenotyping in SARS-CoV-2-infected participants and uninfected controls to define events coordinating innate and adaptive

immunity, convalescent responses, and ongoing inflammation in the setting of persistent symptoms. Participants with a WHO ordinal severity score of 2 or 3 who did not require hospitalization were recruited. Peripheral blood was sampled and analyzed longitudinally by 1) flow cytometry, 2) single cell RNAseq, 3) single cell ATACseq, 4) serum proteomics, 5) serology, and 6) *in vitro* anti-SARS-CoV-2-specific T and B cell responses. Samples were collected from at least 3 timepoints for every participant from 1-121 days post-symptom onset (PSO). We identified multimodal immune features over time that drive interindividual heterogeneity of SARS-CoV-2-specific immune responses, and correlated these with convalescent outcomes including levels of virus-specific memory B cells, antibodies, and occurrence of PASC. Serum protein profiling uncovered unique signatures that defined early acute infection and PASC. Integrative multi-omic analysis suggested key immune regulatory nodes in acute infection, the priming of adaptive immune responses, and PASC. These data provide a unique addition to existing and future COVID-19 related studies, and enable mechanistic hypothesis generation on mild disease progression as well as identifying multiple targets for future validation studies in immunomonitoring natural infections and vaccine-induced immunity.

Results:

Mild COVID-19 shows heterogeneity in clinical presentation and magnitude of acute and SARS-CoV-2-specific immune responses:

We recruited 20 SARS-CoV-2 PCR-positive subjects with mild disease and 23 PCR-negative, uninfected controls from the Seattle metropolitan area. Of the COVID-19 participants, 18 had an initial sample collected less than 15 days from the onset of symptoms so these were selected for full longitudinal analysis (see Methods for inclusion criteria and quality control). The demographics and clinical features of this cohort are provided in **Supplementary Table 1**. Participants were split between younger (<40 years; n=21) and older (≥ 40 years; n=17) age groups (median age 29 vs. 57 years, respectively) (**Fig. 1A**). Each sample was processed in parallel into a multi-omic immunophenotyping pipeline including PBMCs analyzed by flow cytometry, scRNAseq, and scATACseq. Serum was analyzed by Olink proteomics (**Fig. 1B**). Each COVID-19 participant had 3-5 longitudinal study visits including, at a minimum: early acute infection (1-15 days PSO), late acute infection (16-30 days PSO), and post-acute COVID-19 (>30 days PSO) with a median follow-up of 81.5 (range: 33-121) days PSO (**Fig. 1C**). Uninfected controls had only a single study visit. Detailed symptom surveys were performed at each visit and cumulative results are summarized in **Fig. 1D**. Samples were also evaluated for SARS-CoV-2-specific adaptive immune responses by measuring IgG, IgM, and IgA antibody titers to spike (S) protein receptor binding domain (RBD), IgG to nucleocapsid (N) (Stamatatos et al., 2021), focus reduction neutralization assays against an infectious SARS-CoV-2 clone (Vanderheiden et al., 2020), intracellular cytokine staining (ICS) to assess cytokine expression by activating CD4+ and CD8+ T cells with viral peptide pools covering SARS-CoV-2 structural proteins, and measurement of antigen-specific plasmablasts and memory B cells using S and RBD tetramers (**Fig. 1E**).

Illness severity was classified by participant report of impact on activities of daily living for each day of acute illness (U S Department et al., 2017), Corrected Version 2.1). WHO clinical progression scale was additionally used to classify each participant (Marshall et al., 2020). Despite being classified with a score of 2 or 3 on this WHO scale, mild COVID-19 participants had heterogeneous clinical presentations and disease courses. Individuals with any symptom continuing or related to COVID-19 beyond 60 days were classified as PASC. Sources of heterogeneity were primarily recovery time, ranging from 1-32 days of symptoms during acute infection and the spectrum of symptoms (**Fig. 1D**). To better quantify the range of symptom severity within this mild cohort, a novel score was calculated representing the weighted time duration of symptomatic illness severity (see **Methods**). This illness severity score demonstrated the substantial clinical heterogeneity among participants (range 3-141; median 12) (**Fig. 1D**) and was used for further analyses. All COVID-19 participants were symptomatic during acute infection, but the only symptoms shared by the majority of

participants were fatigue or malaise (14/18), dry cough (13/18), headache (12/18), and loss of smell (11/18) (**Fig. 1D**). Most participants resolved symptoms within the acute period, but 3 female participants had persistent symptoms and were diagnosed with PASC.

The majority of donors mounted measurable SARS-CoV-2-specific adaptive immune responses. Antigen-specific CD4+ and CD8+ T cell responses targeting envelope (E), membrane (M), N, S, and open reading frame (ORF) 3, 6a, 7a, 7b, and 8 proteins peaked at approximately day 30 and did not appreciably decline in most participants (**Fig. 1E**). Frequencies of SARS-CoV-2-specific CD4+ T cells were consistently higher than CD8+ T cells within the same donor. Antibody responses were also analyzed for all participants, including neutralizing antibody and RBD-specific IgG titers (**Fig. 1F**): RBD-specific IgG titers peaked around day 30, while neutralizing antibodies peaked slightly later. While 100% (18/18) of COVID-19 participants mounted a sustained RBD-specific IgG response, only ~70% (13/18) sustained neutralizing antibody responses after acute infection. Spike-specific plasmablasts and IgG+ memory B cells were also detected in most participants (**Fig. 1G**). Peak plasmablast responses occurred within the first 15 days after onset of symptoms followed by a rapid decline by 30 days PSO in most participants. Spike-specific class-switched IgG+ memory B cells were also detected in all participants and generally increased in frequency over time. Antibody titers, and frequencies of CoV-2-reactive B and T cells were fit to linear mixed-effects models using data >30 days PSO to estimate peak SARS-CoV-2 adaptive responses for each participant.

Next, we performed pairwise correlation analysis to identify connections among and between SARS-CoV-2-specific immune responses at day 30 PSO, demographic features, and clinical disease course (**Fig. 1H**). PASC was positively correlated with an increased number and variety of symptoms (muscle aches or pains, fatigue or malaise, nausea or vomiting, diarrhea, loss of smell, changes in taste). Unexpectedly, PASC was negatively correlated with several adaptive responses including SARS-CoV-2-specific CD8+ T cells, RBD- and S-specific total memory B cells (sum of IgG+, IgM+(IgD-), IgA+), and N IgG and RBD IgM titers, suggesting association between PASC and lower virus-specific immune responses (see **Fig. 4**). Age was positively correlated with both antigen-specific CD4+ and CD8+ T cell responses as seen in the broader cohort analysis (Cohen et al., 2021). These results led us to perform an additional exploration of age-associated effects in this mild COVID-19 cohort and to perform a deeper analysis of participants with PASC.

Early acute SARS-CoV-2 infection is characterized by an activated, inflammatory state including age-enhanced IFN responses and plasmablast expansion:

We sought to define the immune response in mild COVID-19 during early acute infection, here ≤15 days PSO. Global unsupervised principal component analysis of the serum proteome showed significant differences between COVID-19 participants and uninfected controls (**Fig. S1A**). We compared early acute COVID-19 infection to uninfected controls and identified 404 differentially expressed proteins (**Fig. 2A; Supplementary Table 2a**). The serum proteome suggests a coordinated innate immune response that is dominated by type I IFN-related antiviral responses and pro-inflammatory cytokines (tumor necrosis factor, TNF; IL-18). The most differentially increased protein was RIG-I, an innate sensor encoded by the gene *DDX58* that detects double-stranded RNA viruses and drives expression of type I IFNs. RIG-I is known to restrict SARS-CoV-2 infection of pulmonary epithelial cells via type I/III IFN responses (Yamada et al., 2021). FKBP5, a product of the acute stress response, was also differentially increased and was recently shown to regulate RIG-I signaling in response to influenza infection (Hao et al., 2020a). Upregulation of SAMD9L, a host restriction factor for poxviruses and an ISG, is also preferentially induced by type I IFNs (Pappas et al., 2009). Increased IFNL1 and IFNLR1 suggested type III IFN responses were also induced. Many of the proteins that were differentially increased overlap with the serum proteome reported in hospitalized and severe COVID-19 (Filbin et al., 2020). Strikingly, severe participants demonstrate a pronounced increase in IFNγ expression and increased type II IFN-driven protein expression. In contrast, IFNγ was not elevated in our cohort, suggesting a less pronounced type II IFN-driven response may distinguish mild from severe COVID-19.

Cellular immune changes were assessed during acute infection by first analyzing proportions of innate and adaptive immune cell types and expression of phenotypic surface markers by flow cytometry. Principal component analysis of cell type frequencies showed significant differences between COVID-19 participants and uninfected controls (**Fig. S1B-C**). Plasmablasts and PD-1high CXCR5- T peripheral helper (Tph) cell frequencies were most significantly increased in COVID-19, while naive (IgD+IgM+) B cells were significantly decreased (**Fig. 2B)**. Activation marker-positive B and T cells were also significantly increased, including CD69 and PD-1 on non-naive CD4+ T cells, CD69 and CD38 on CD8+ T cells, and BCMA, CD71, CD86, and CD319/SLAMF7 on plasmablasts and B cells. These changes demonstrate coordinated immune activation across adaptive and innate immunity in acute infection. scRNAseq provided deeper phenotyping of transcriptional state to analyze cell type activation. Cells were labeled by mapping scRNAseq to a CITE-seq-based multimodal reference atlas (Hao et al., 2020b), and resulting proportions were significantly correlated with flow cytometry (**Fig. S1D-H**). Proliferating lymphocytes (CD71+ CD4+ and CD8+ T cells, CD71+ NK cells; **Fig. S2A**) were also significantly upregulated in mild COVID-19 infection, consistent with previous reports of a proliferating T cell phenotype in more severe COVID-19 (Stephenson et al., 2021).

Age is a well-known risk factor in COVID-19 that is associated with many compositional and functional changes (Channappanavar and Perlman, 2020; Richardson et al., 2020; Takahashi et al., 2020). Older COVID-19 participants (≥ 40 years old) had higher proportions of innate and adaptive immune cell types during early acute infection, including central memory CD4+ T cells (TCM), memory Tregs and CD14+ monocytes, while younger participants (<40 years old) had higher naive CD8 T cells and naive Tregs (**Fig. S2B**). Elevated serum levels of inflammatory cytokines (IL6, IL18BP) and chemokines (CCL8, CXCL10) were detected in older compared to younger COVID-19 participants during early acute infection (**Fig. S2C**). Functional analysis of cells using scRNAseq showed robust IFN responses in all cell types from older COVID-19 participants (**Fig. S2D-E, Supplementary Table 2B**) compared to uninfected controls. In contrast, only CD14+ monocytes and CD56bright NK cells showed IFN responses in younger COVID-19 participants (**Fig. S2E**). Comparing the fold-change of these responses between older and younger COVID-19 participants revealed that IFN responses were significantly higher in all analyzed cell types from older participants (**Fig. 2C, Fig. S2F, Supplementary Table 2C**), with the greatest age-associated enhancement in the monocyte and NK populations. Differentially expressed ISGs showed a clear gradient that increased with age and did not vary across cell types: uninfected participants had the lowest ISG expression, followed by higher expression in younger COVID-19 participants, and highest expression in older COVID-19 participants (**Fig. 2D**). While IFN responses were significantly activated in diverse PBMCs by gene expression, only IFNL1 (type III) was elevated in COVID-19 serum. Other inflammatory cytokine signaling pathways were also up-regulated in diverse cell types from older participants (**Fig. 2C**). TNF response was most prevalent behind IFN responses, with age-enhanced responses in monocytes, CD56bright and proliferating NK cells, DCs, CD4+ T cells, and B cells. IL1 signaling pathways were also significantly up-regulated in older participant cell types, which may reflect inflammasome activation in early acute infection.

Transcription factor motif analysis on scATACseq was used to identify the most active cell types in acute infection, and any differences associated with age. Plasmablasts and innate immune cells (DCs, monocytes) had the largest motif shifts from uninfected controls (**Fig. S2G**). AP-1, a regulator of stress response and immune activation, was significantly enriched in innate immune cells, particularly CD14+ and CD16+ monocytes in older and younger participants, and DCs in older participants (**Fig. S2H**). AP-1 enrichment was also observed in some effector cell types (proliferating NK cells, CD8+ TEMRAs) in older participants. These observations are consistent with scRNAseq and proteome data showing increased inflammatory cytokine responses that could activate AP-1. Strong IFN responses were also observed via enrichment of IRF motifs, particularly in plasmablasts.

One of the most striking differences in early infection was the increased abundance of circulating plasmablasts, which has typically been reported in more severe COVID-19 (Arunachalam et al., 2020; Kuri-Cervantes et al., 2020; Mathew et al., 2020). Plasmablast proportions by flow cytometry and scRNAseq were

significantly higher in COVID-19 participants ≤15 days PSO when compared to uninfected controls (**Fig. 2b, Fig. S2A**). Our data demonstrated that a high portion of the plasmablast expansion in mild SARS-CoV-2 was S-specific (**Fig. 1G**). Plasmablasts from younger COVID-19 participants compared to uninfected controls were enriched for RAD12 and CTCF motifs, and were strongly depleted for TCF family and RUNX motifs. Consistent with age-enhanced IFN responses, we found IRF family motifs were significantly enriched in plasmablasts from older participants (**Fig. 2E,** left panel). In contrast to plasmablasts, DCs had the second highest magnitude change in motifs, but showed few age-associated changes (**Fig. 2E**, right panel): all participants showed enrichment of AP-1 and HMG (HMGN2, TCF7L2) family members, and depletion of RUNX and SPI family motifs. These results suggest a potential link between IFN and plasmablast responses to acute infection by SARS-CoV-2.

We inferred ligand-receptor (LR) interactions from plasmablast transcriptomes during early acute infection to define the upstream signals that may drive their response (Browaeys et al., 2020) (**Fig. 2F**). The top ligands identified as inputs into early plasmablasts included type II and III IFNs (IFNG, IFNL1), TNFRSF13B/TACI, and CD40LG (AUROC>0.58). Potential PBMC sources were identified including innate immune cells for TNFSF13B and MAIT and γδ T cells for CD40LG. IFNG and IFNL1 had no putative PBMC sources identified, again suggesting tissue sources may be the primary source for IFNs in early acute infection. STAT1 was identified as a shared downstream target node for these ligand-receptor interactions (**Fig. 2F**; **Supplementary Table 2D**), consistent with strong IFN responses. These results support generation of mechanistic hypotheses for key signals identified in other studies, such as the role of early IFNL1 in mild COVID-19 (Galani et al., 2021). Our data suggest early IFN responses, particularly IFNL1, may drive plasmablast responses, potentially through synergy with BCR (Syedbasha et al., 2020) and TLR signaling (de Groen et al., 2015), and this may link early control of viral replication, inflammatory cytokine milieu, and extrafollicular B cell responses. Future studies will be critical to confirming the function of these plasmablasts in SARS-CoV-2 infection.

Longitudinal analysis shows that a decrease in activated and proinflammatory responses correlated with an increase in repair and convalescent homeostasis pathways:

After defining unique characteristics of early acute infection, we analyzed significant longitudinal changes in immune phenotype during mild COVID-19. Serum proteins that significantly decreased over time were largely proinflammatory proteins, including cytokines (IL18, TNF), chemokines (CCL8, CCL7, CXCL10), complement proteins (C4BPB, C2), and IFNL1 (**Fig. S3A**). These proteins were enriched for type I and II IFN responses, TNF signaling, interleukin (IL-1, IL-2, IL-6) signaling, and innate immune sensor (Toll-like receptor, TLR; Nod-like receptor, NLR) signaling (**Fig. 3A, Supplementary Table 3A**). Inflammatory protein changes detected during acute infection resolved around day 30 PSO for most COVID-19 participants. A subset of proteins, including the anticoagulant thrombomodulin (THBD), angiogenic factors, and proteins involved in tissue remodeling increased over time. These were enriched for epithelial-mesenchymal transition (EMT), angiogenesis, and coagulation pathways, showing that convalescence is characterized by a transition to a wound healing, homeostatic phenotype from the inflammatory response in acute infection (**Fig. 3A**). Some chemokines increased over time, including CCL21, which can drive lymphocyte migration to sites of inflammation and homeostatic lymphoid trafficking, and CCL16, an IL-10 inducible chemokine that can serve both proinflammatory and immunoregulatory functions, and is consistent with previous observations of CCL16 depletion during acute infection in severe COVID-19 (Filbin et al., 2020). While most COVID-19 participants resolved proteome changes around 30 days PSO, the inflammatory responses in PASC participants (red PASC column annotation) persisted (**Fig. 3A**).

Cell proportions measured by flow cytometry mirrored the proteome, with most changes during acute infection resolving by 30 days PSO. These included decreases in plasmablasts, Tph cells, and CD14+ CD16+ intermediate monocytes, and activation marker-positive B and T cells (**Fig. 3B**). CD1c+ DC2s and CD4+ TCMs increased over time, consistent with a return from virus-infected tissues for DC2s (Bosteels et al., 2020; Gill et

al., 2008) and expansion or differentiation of CD4+ TCM cells after acute infection. BAFF-R+ class-switched memory B cells and IgG+ B cells increased over time, which suggests recent memory differentiation and class-switching from activated B cells during acute infection (Lau et al., 2021). IgA+ plasmablasts also increased over time and may be a consequence of acute infection-induced plasmablasts contracting. Proliferating lymphocytes identified in scRNAseq also significantly declined over time (**Fig. S3B**).

To assess coordination of the immune response, we correlated the change in cell type proportions measured by flow cytometry and scRNAseq with changes in the serum proteome over time (**Fig. S3C**). Cell types that positively correlated with the activity of the most serum proteome pathways included CD14+ CD16+ monocytes, Tph, memory B cells, and proliferating lymphocytes (**Fig. 3C**). Decreases in these cell type proportions over time were associated with decreased type I and II IFN responses, inflammatory cytokine and immune activation signaling, and PRR signaling. In contrast, these decreases were correlated with increases in BAFF-R+ B cells and serum proteome pathways for chemokines, wound healing, and tissue repair, suggesting temporal coordination between inflammatory resolution and homeostasis characterizes successful recovery from mild COVID-19.

We next used scRNAseq and scATACseq data to longitudinally map cell type-specific changes in function over time. Genes demonstrating significant changes over time were identified per cell type, then mapped changing genes to their corresponding pathways. Pathways that showed the top enrichment scores and were most decreased over time, as weighted by number of impacted cell types and participants (see Methods), included TNF signaling, IFN responses, TLR signaling, and apoptosis (**Fig. 3D, Fig. S3D, Supplementary table 3B**), and these were consistent with inflammatory protein decreases in serum. Innate immune cells (monocytes, cDC2s, NK subsets) were the majority of the top cell types expressing these longitudinally changing pathways. scATACseq showed that most transcriptional motifs enriched in acute infection rapidly declined in activity over time, as demonstrated by IRF family motif shifts (**Fig S3E**). AP-1 motifs were among the most accessible features in innate immune cell types during early acute infection for nearly all COVID-19 participants (**Fig. S2H**). Accessibility of AP-1 motifs peaked in CD14+ monocytes during acute infection, followed by rapid decline to homeostatic baseline by 30 days PSO (**Fig. 3E**). PASC participants were a notable exception, maintaining higher accessibility >30 days PSO, which may represent persistent innate immune activation. Principal coordinates analysis (PCoA) on longitudinally changing immune features revealed the individual trajectories of COVID-19 participants from acute infection through convalescence (**Fig. 3F**). Early acute infection samples (black circles) showed clear differences from uninfected controls (light green circles, **Fig. 3F**, top inset left), while most participants around 30 days PSO were closer to uninfected controls (**Fig. 3F**, bottom inset left). COVID-19 participant trajectories (lighter colored circles and arrows) converged closer to the uninfected control space by ~30 days PSO (**Fig. 3F**, middle panel). Distances for each sample were calculated from the centroid of the uninfected control group to visualize the timing of inflammatory resolution (**Fig. 3F**, right panel). Most participants' trajectories resolved near uninfected controls around day 30, with notable exceptions for two of three PASC participants who remained >2.5 distances from the uninfected group. Overlaying comorbidity annotations on the PCoA revealed that the PASC participant with the most comorbidities had the most distinct trajectory from other COVID-19 participants (**Fig. S3F**). Altogether, longitudinal analyses across data types demonstrated that most mild COVID-19 participants resolved into a convalescent immune phenotype similar to uninfected controls, while PASC participants have persistent differences and unique trajectories.

PASC participants are distinguished by dampened anti-viral and IFN responses in acute infection and persistent, unresolved inflammatory signaling in convalescence

Recovered COVID-19 participants had no symptoms after ~2 weeks PSO (range: 0-17 days PSO). There were however, 3 participants with continued symptoms lasting for > 60 days PSO, who were classified with PASC (**Fig. 4A)**. All PASC participants were female, similar to the sex bias reported in previous studies (Davis et al., 2020; Evans et al., 2021; Sigfrid et al., 2021). Two participants had more severe illness and

persistent symptoms including cognitive impairment (PTID 795172; illness severity score 71, WHO score 3) and cardiovascular abnormalities (PTID 523731; illness severity score 141, WHO score 3). A third PASC participant (PTID 285840, illness severity score 3, WHO score 2) showed mild illness during acute infection, but presented with myriad chronic symptoms including joint swelling, tingling, chest pain, abdominal pain, and loss of smell (**Supplementary Table 1A**). Follow-up is ongoing for all PASC participants, and at present, symptoms have persisted for >270 days PSO. PASC participants had qualitative differences in CoV-2-specific responses (**Fig. 4B**), but none were statistically significant, likely due to the small sample size. There are however trends suggesting that PASC participants may have dysregulated adaptive immune responses. Most notably, all 3 PASC participants had low or absent SARS-CoV-2-specific CD8+ T cells after 30 days PSO. Two of the three also had SARS-CoV-2 response estimates below the lower quartile of recovered COVID-19 participants for RBD- and S-specific memory B cells, RBD IgG, N IgG, and RBD IgM (**Fig. 4B**).

To further identify immune pathways and cell types that may differentiate PASC from participants who had an uneventful recovery from acute SARS-CoV-2 infection, we evaluated scRNAseq data from both groups of participants. Differentially expressed genes (DEGs) were identified by comparing PASC participants to recovered COVID-19 participants ≤15 days PSO by cell type. CD14+ monocytes, CD8+ effector memory T cells (CD8+ TEM), and CD16+ monocytes showed the highest number of DEGs (**Fig. S4C**). Mapping DEGs to pathways by cell type revealed dysregulated signaling in early acute infection that persisted longitudinally in PASC. Consistent with evidence of dysregulated immune responses described above, early infection in PASC was characterized by significantly lower RIG-I signaling and IFN responses compared to uninfected controls in CD14+ and CD16+ monocytes, and CD8+ TEM cells (**Fig. 4D, Fig. S4F**). These signatures remained persistently low throughout disease, while levels in recovered participants increased during acute infection and dropped over time. Co-expressed genes from these pathways defined an antiviral response module that was impaired in PASC compared to recovered participants (**Fig. S4G).** At the same time, CD14+ monocytes (**Fig. 4D, Supplementary Table 4B**) and CD8+ TEM cells (**Fig. S4D**) demonstrated increased expression of pro-inflammatory genes that was significantly higher in early acute infection from PASC compared to recovered participants, and persisted throughout the course of infection. The up-regulated genes included *IL1B*, *RIPK2*, and AP-1 transcription factor subunits (*FOS* and *JUN*), components of gene modules associated with TNF signalling and hypoxia (**Fig. S4E**).

The presence of an inflammatory gene signature led us to examine whether there are specific circulating immune mediators that correlate with ongoing symptoms in PASC. We performed outlier analysis on the longitudinal serum proteome to identify signatures that distinguished PASC from recovered COVID-19 participants. Most recovered COVID-19 participants (14/15) had a decreasing number of differential proteins over time compared to uninfected controls indicating their path back to normalcy. Two of the 3 PASC participants had stable or increasing numbers of differential proteins over time (**Fig. S4A**). A signature of persistently elevated inflammatory signals distinguished PASC participants from recovered COVID-19, including IL-5, S100A16, CD74, IFNLR1, and CD28 (**Fig. 4C).** Due to the small sample size, we looked at a broader signature of 132 differentially expressed proteins (**Fig. S4B**, $p<0.05$) that distinguished PASC from recovered participants. Upregulated proteins were enriched for those in functional pathways associated with inflammatory responses including respiratory burst, T cell antigen processing, innate response in mucosa, and others (**Supplementary Table 4A**). Among the larger set of differentially expressed proteins, a number of TNF superfamily members were upregulated proteins in severe PASC, including TNSF10/TRAIL, TNFRSF4/CD134, TNFRSF9/4-1BB, and TNFRSF11B, consistent with an immune activation phenotype. In addition, two immunosuppressive checkpoint proteins (LAG3, PDCD1/PD-1) were upregulated in more severe PASC, which may result from excess T cell activation and could limit adaptive immune responses to viral infection and increase illness severity (Saheb Sharif-Askari et al., 2021). Hierarchical clustering of differentially expressed proteins showed that the two more severe PASC participants (PTIDs 795172, 523731) clustered together, while the third (PTID 285840) showed a distinct, less inflammatory signature (**Fig. S4B**). Overall, analysis of

the serum proteome in this limited set of PASC participants suggests a hyperinflammatory state that is most prominent in the two more severely affected individuals.

In an effort to understand whether there are particular immune cells either driving or responding to the signals identified in the serum proteomic studies, we performed transcription factor (TF) motif analysis of scATACseq data. This revealed key TF motifs that correlate with aberrant cell phenotypes in PASC participants compared to COVID-19+ recovered participants at >30 days PSO. A set of AP-1 family motifs were significantly enriched in dendritic cells (DCs) and CD14+ monocytes. Paired with evidence of increased expression of the genes encoding the AP-1 subunits FOS and JUN, this suggests a state of persistent immune activation that is most prominent in innate myeloid cells (**Fig. 4E**). Other prominent enriched motifs included BACH, BATF, IRF, and STAT families, all associated with persistent inflammatory cytokine signaling. The same motifs were also enriched, albeit to a lesser extent, in CD4+ TEM and CD8+ TEMRAs. Motif enrichments were not observed across all innate immune cells or for most adaptive immune cell types in PASC.

To identify potential signals driving the phenotype of CD14 monocytes in PASC, scRNAseq gene expression changes were used to predict ligand-receptor interactions by the NicheNet method (Browaeys et al., 2020). Ligand activity was predicted and ranked by the correlation between knowledge-based predictions and experimentally observed levels of target gene expression (**Fig. S4H**). Ligand expression was assessed in all cell types along with the fold increase in their expression per cell type compared to recovered subjects to identify PBMC sources of ligand signals (**Fig. S4I)**. TNF, NAMPT and IFNγ were the top 3 predicted ligands with highest target gene activity in CD14 monocytes (**Fig. S4H, S4J, 4F**). Diverse potential sources for these ligands among PBMCs included proliferating CD8+ T cells, CD8 TEMRA, CD4 CTLs, DCs, and monocytes (**Fig. S4I)**. Target genes of these predicted ligands included *IL1B*, *FOS*, *NAMPT*, *BCL2A1*, *PLAUR*, and *HIF1A* (**Fig. 4F, S4J**), which confirm observations in **Fig 4D and Fig. S4E**. Differential signaling may be induced without serum-level changes in ligand abundance, since immune cells may integrate signals dependent on spatial context and from tissues before circulating in blood. scRNAseq analysis was consistent with this, by providing evidence of elevated TNF signaling in CD14 monocytes even in the absence of significant TNF upregulation in serum. Overall, these data suggested a key role for the cytokine milieu driving a persistently proinflammatory state in CD14+ monocytes, identifying biomarkers for diagnosis of PASC, and revealing multiple therapeutic targets.

These results suggest that PASC is characterized by blunted innate and adaptive antiviral immune responses during acute infection, paired with emergence of a persistent inflammatory state that includes increased expression of pro-inflammatory genes and proteins. Dendritic cells and monocytes demonstrate the most significant changes in chromatin accessibility including binding motifs for AP-1, STAT, and IRF transcription factors known to play important roles in inflammatory gene transcription. It is unclear whether this serves as a primary driver of the phenotype observed in PASC or is the result of persistent activation by circulating inflammatory mediators arising from another source.

Heightened early acute interferon and antiviral signaling correlate with stronger humoral responses to SARS-CoV-2 in convalescence:

Antibody responses are a key component to controlling viral infection, disease outcome, and protection from reinfection. Clinical trials have directly shown that neutralizing antibodies (nAb) to SARS-CoV-2 can reduce mortality and length of hospitalization (Chen et al., 2021). Immune responses in acute infection are critical for establishing the coordinated immune response required for development of antibody and memory B cell responses in convalescence. Serum protein expression and flow cytometry proportions were estimated at day 7 PSO. RBD IgG titers and S-specific memory B cell frequencies at day 30 PSO and neutralizing antibody (nAb) titers at day 42 PSO were estimated by linear mixed-effects models. Observed and estimated values were strongly correlated (**Fig. S5A, S5B**).

We identified a signature of circulating proteins, present during early acute infection (day 7 PSO), that strongly correlated to peak antibody titers for RBD IgG and neutralizing antibody (nAb) at days 30 and 42 respectively

(**Fig. 5A, 5B**). A circulating protein signature was also identified that correlated with spike-specific memory B cell frequencies (**Fig S5C**). Correlations were also found between specific immune cell subsets identified by flow cytometry and RBD IgG, nAb, and the S-specific memory B cell frequency (**Fig. 5D, 5E; Fig. S5D**). Analysis of the serum protein milieu at day 7 PSO revealed that higher expression of proteins in inflammatory pathways were significantly correlated with higher RBD IgG titers at day 30 PSO. Among the most prominent were ISGs (TRIM21, SAMD9L), complement (CD55, GPB1A), and innate sensor signaling proteins (TANK, MAVS, RIG-I) (**Fig. 5A**). Neutralizing antibody titers at day 42 were also positively correlated with day 7 innate immune proteins (IFNλ1, DDX58), while negative correlates included a subset of inflammatory proteins (IL-34, IL-17A, CD209/DC-SIGN) and chemokines (CCL15, CCL28) (**Fig. 5B**). These underscore the importance of innate immunity in early infection for encoding the magnitude of the convalescent antibody response. Sixteen serum proteins were common correlates for both RBD IgG and nAb (**Fig. 5C**), but these did not share any functional pathways. Soluble correlates were complemented by positive correlations with flow cytometry populations, including selected activation marker-positive T cells (PD-1+/TIGIT+) and naive B cells (IgD+IgM-), as well as CD56high NK cells (**Fig. 5D**). This links the magnitude of humoral response to the degree of T and B cell activation, potentially through support of B cell maturation to plasma and memory cells. Negative correlates of RBD IgG included pre-switch memory B cells (CD27+IgD+), and CD11b+ B cells. Cell proportions that positively correlated with nAbs included circulating CXCR5+ PD-1+ Tfh cells, and CD56high and CD16- NK cells. Phenotypic markers of activation on T cells (CD38, CD71, PD-1) and plasmablasts (BCMA) were positively correlated with neutralizing titers. Negative correlates of neutralizing titers included naive CD4+ T cells and inhibitory receptor-positive (KLRG1, TIGIT) CD56low NK cells (**Fig. 5E**). Coordination of multiple aspects of immunity (lymphocyte activation, innate immune signaling) in early infection are strong predictors of effective priming for IgG and neutralizing antibody responses against SARS-CoV-2.

A critical role for memory B cells has been posited to provide rapid protection upon rechallenge (Dan et al., 2020). We identified serum proteins and cell frequencies from early infection that correlate with convalescent S-specific IgG+ memory B cell responses. Similar to IgG titers, we observed strong positive correlations with secreted proteins enriched in innate immunity, IFN responses, and RIG-I signaling (**Fig. S5C**). In contrast, proteins negatively correlated with memory B cells included complement, chemokines (CCL16, CCL20), and interleukin (IL-1, IL-2) signaling. Cell frequencies that positively correlated with memory B cell response included DC2s and CD25- ILCs, and activated plasmablasts and memory B cells (BCMA) (**Fig. S5D**). KLRG1 on non-naive CD4+ T cells and PD-L1 on CD14+CD16+ intermediate monocytes were also positively correlated with memory B cell responses. Overall, these findings identified diverse cellular and molecular features of early infection that correlate with antibody and memory B cell responses, identifying candidates for immunomonitoring and novel linkages between the acute antiviral response and the magnitude of humoral immune responses.

Integrative analysis reveals key network nodes in acute SARS-CoV-2 infection, their longitudinal resolution, and persistence in PASC:

We sought to trace the longitudinal resolution of immune signals that characterized acute infection through longitudinal resolution and convalescence. Several serum inflammatory proteins that were elevated during acute infection had prolonged elevation in PASC participants, including IL-1β, IL-5, IL-6, and TNF (**Fig. 6A**). To infer the origin and signaling activity of these proteins, we performed intercellular communication analysis of scRNAseq data using NicheNet (Methods). We first identified cell type-specific expression of proteins from acute infection (from **Fig. 6A),** determined candidate secreting/sender cell types for these signals **(Fig. S6A)** to define the ligand-cell type interaction network in PBMCs from acute infection (**Fig. 6B**, 31 predicted ligands in >10% of all cell types). Ten cell types were analyzed as potential receivers of signals based on their changes observed in early acute infection (**Figs. 2, 3**): plasmablasts, CD14 monocytes, CD16 monocytes, NK cells, proliferating cells (CD4, CD8, NK), and DCs (DC1, DC2, pDC). The top 10 high-confidence predicted ligands among these receiver cell types were determined (**Fig. 6C**) and ranked based on

the percent of cell types with predicted ligand activity. These ligands demonstrated the prevalence of inflammatory signaling, including IFN, IL, and TNF family members (**Supplementary Table 5A; Fig 6B-D**). These predicted ligands converged onto a shared downstream target gene, *STAT1* (**Fig. 6D**) as well as *DDIT4* (regulator of mTOR, proliferation, autophagy), and multiple other transcriptional regulators (*NFKBIA*, *JUN*, *FOS*).

Next, we analyzed LR interactions of differentially expressed target genes from 3 distinct comparisons: 1) early acute infection compared to uninfected, 2) longitudinal timepoints (>15 days PSO) compared to early acute infection, and 3) PASC participants (all timepoints) compared to recovered COVID-19. There was significant overlap of LR pairs (567 pairs, 27%) identified in early acute infection, longitudinal timepoints, and PASC participants (**Fig. 6E, Supplementary Table 5B**), indicating common signals driving each subset of mild COVID-19. Early acute infection had the highest number of unique LR interactions (461 pairs, 22.2%) followed by PASC (291 pairs, 14%), and longitudinal timepoints (175 pairs, 8.4%). Notably, a subset of LR interactions (77, 3.7%) were shared between early acute infection and PASC, which may represent signals from acute infection that persist abnormally in PASC. We dissected LR usage by participant subgroup to identify ligands and targets that were more abundantly used in PBMC networks for early acute infection, longitudinal resolution, and PASC (**Figs. 6F, G**). Innate immune signals and inflammation signaling from early acute infection compared to uninfected controls persisted in PASC compared to recovered COVID-19 participants (**Fig. 6A**). Increased activity for some predicted ligands in PASC participants were consistent with elevated levels in the serum proteome, including LTA, MDK, CXCL5, and MIF (**Fig. 6F, Supplementary Table 5C, S6C**). A subset of downstream gene targets from predicted ligands was used in all 3 subgroups, and primarily consisted of genes coding intracellular proteins: *DDIT4, NFKBIA,* and *CDKN1A* (**Fig. 6G**). PASC networks were enriched for downstream target genes encoding for transcription factors (*CEBPB*; *IRF4*; AP-1 subunits *FOS* and *JUNB*) and secreted proteins including *IL1B* and *VEGFA*. Persistent activity of transcription factor targets was also supported by scATACseq data, where C/EBP-β and AP-1 motifs were increased in monocytes and DCs from PASC participants compared to recovered COVID-19 after day 30 PSO (**Fig. 4E**). Among secreted proteins, IL-1β was one of the most broadly predicted signals and downstream targets in PBMCs from PASC participants (**Figs. 6F, G**). The signal landscape from PASC suggests neutralizing soluble proteins such as TNF, LTA, or IL-1β after acute infection could offer a potential therapeutic approach. Additionally, PASC may be characterized by activation of stress response programs as evidenced by AP-1 and *DDIT4*, which may be signs along with IL-1β of an imbalance between autophagy and inflammasome activation. Overall, network analyses provide a platform for mechanistic hypothesis generation on key active pathways in mild COVID-19 from acute infection through resolution that may prime adaptive immune responses, influence disease outcome, and enable diagnosis and treatment of complications such as PASC.

Discussion:

Our study provided an in-depth longitudinal analysis of the immune response to SARS-CoV-2 natural infection and mild COVID-19 by integrating serum proteomics, single-cell transcriptomics and epigenomics, and cellular immunophenotype by flow cytometry with clinical metadata and comprehensive analysis of the SARS-CoV-2-specific adaptive immune response in T cells, memory B cells, and antibodies. To our knowledge, this is the deepest longitudinal systems immunology study to-date in mild COVID-19, and reveals numerous new insights. First, we define the immune response to early acute infection including inflammatory cytokine and innate sensor signaling, stronger IFN responses in older participants, and a potential IFN-plasmablast regulatory circuit. A subset of these changes were correlated with the humoral response to SARS-CoV-2 in convalescence. We then confirmed the longitudinal resolution of these inflammatory pathways was coordinated with re-establishment of homeostasis in most participants. Three PASC participants were exceptions to this resolution, and could be distinguished by dampened IFN and antiviral response in acute infection coupled with prolonged inflammation. Finally, we integrated these data to identify potential master

regulatory nodes in early infection, longitudinal resolution, and PASC for hypothesis generation and validation of biomarkers and therapeutics.

A defining characteristic in our mild COVID-19 cohort was robust immune activation in the first 2 weeks of acute infection that resolved over time. This included inflammatory cytokine responses (IFNs, TNF), innate immune sensor signaling pathways, and activation in adaptive and innate immune cells. The key innate immune sensors triggered in natural SARS-CoV-2 infection are not confirmed, but multiple data types strongly implicate RIG-I. Serum proteomics identified increased extracellular levels of multiple PRR pathway members including RIG-I during acute infection, but their source and function are unclear. These may derive from recent cell death or extracellular vesicles, which have been reported to potentially transfer TLRs between cells (Zhang et al., 2019). Innate danger sensors are key drivers of the IFN response, which was also robustly induced in our cohort along with other inflammatory signals such as TNF. A subset of upregulated proteins (SAMD9L, CXCL10, CXCL11) is selective to type I/II IFN responses, suggesting bias away from type III IFNs systemically (Allenspach et al., 2021; Forero et al., 2019). As these pathways waned over time, activation marker-positive cells and inflammatory proteins largely returned to uninfected control levels around day 30 PSO. This temporal control is likely critical for successful resolution of mild COVID-19. This contrasts with persistent CRS reported in severe COVID-19, which includes mechanisms of inflammatory damage to tissue such as TNF/IFNγ-mediated cell death (Karki et al., 2021). Proteins involved in homeostatic functions (EMT, coagulation, angiogenesis) increased from acute infection to convalescence. The longitudinal increase of multiple coagulation pathway proteins may contribute to reported increases in risk of immune thrombocytopenia, a complication associated with severe COVID-19 infection (Guan et al., 2020). We found levels of THBD were significantly increased in convalescence of mild COVID-19, and has been reported to strongly correlate with duration of hospitalization and risk of mortality in hospitalized COVID-19 (Goshua et al., 2020). These results suggest a link between the inflammatory response in acute infection, the kinetics of inflammatory resolution, and their dysregulation in long-term coagulopathy risk and severe COVID-19.

We observed a clear increase in immune responses with advancing age in mild COVID-19. Age is among the strongest risk factors for severe COVID-19 and mortality, but the mechanisms underlying these effects remain poorly defined (Williamson et al., 2020). Many studies are confounded by age when comparing younger controls and mild COVID-19 cases with typically older individuals in moderate and severe COVID-19. A male-specific age effect was correlated to poorer CD8+ T cell responses and disease severity with advanced age (Takahashi et al., 2020). Our cohort was age-matched between COVID-19 participants and uninfected controls, and age was not significantly correlated with illness severity score. However, IFN responses showed a dramatic age-related effect in increased responsiveness of PBMCs from older COVID-19 participants to IFNs, as evidenced by both more pathway enrichment and higher enrichment scores from scRNAseq, and cell type-specific enrichment of IRF motifs in scATACseq. Enhanced IFN in older participants is contrary to expectations from prior studies on inflammaging, where advanced age is associated with impaired IFN responses (Molony et al., 2017; Pillai et al., 2016). Older participants also showed increased cytokine and danger sensor signaling in innate immune cells. These observations could be due to cells from older participants being more intrinsically reactive to cytokines, the magnitude of inflammatory cytokine response being higher, or persistence of inflammatory cytokines longer in older participants. We also observed increased adaptive immune cell activation, which contrasts with expectations from prior studies showing immunosenescence in elderly healthy individuals. Differences between our results and prior studies on age-related effects in immunity may be due to our cohort including more young and middle-aged adults <55 years old compared to elderly adults typically >65 years old. Collectively, our results indicate that SARS-CoV-2 infection triggers enhanced inflammatory responses in older individuals in mild COVID-19, which may underlie increased risk for severe COVID-19 in older populations.

Robust plasmablast expansion is a feature of viral infections (dengue, Ebola), vaccines, and chronic autoimmune diseases (Kim et al., 2016; McElroy et al., 2015; Wrammert et al., 2012). Previous studies in moderate and severe COVID-19 reported robust plasmablast and extrafollicular B cell responses (Bernardes et

al., 2020; Kaneko et al., 2020; Kuri-Cervantes et al., 2020; Mathew et al., 2020; Ren et al., 2021; Stephenson et al., 2021; Woodruff et al., 2020). We also observed a robust plasmablast expansion in acute infection. A fraction of these plasmablasts were CoV-2 spike protein-specific, indicating these cells can in principle contribute to early control of viral replication and are at least partly CoV-2-specific. PD-1high CXCR5- Tph cells were also positively correlated with plasmablasts, potentially providing help as observed in autoimmune diseases (Rao et al., 2017). IFN responses are among the key drivers of extrafollicular B cell subsets in autoimmunity (Manni et al., 2018; Soni et al., 2020), which was consistent with scRNAseq data showing enhanced IFN signaling and scATACseq data showing IRF motif enrichments in plasmablasts. The functional consequence of these plasmablasts in SARS-CoV-2 infection remains unclear, but may connect IFN responses to antibody titers.

Priming of adaptive immunity is critical to successful resolution of acute infection and protection against reinfection. We found the magnitude of RBD IgM and CoV-2-specific CD4+ T cells negatively correlated with severity score, suggesting quality of immune response may be one driver of clinical heterogeneity in mild COVID-19. IgA titer was also correlated with severity score, extending prior observations that correlated IgA with disease severity (Ma et al., 2020; Ravichandran et al., 2021). Correlates from acute infection were also identified that explain interindividual heterogeneity in magnitude of humoral immune responses. Serum proteins involved in innate immune pathways, including IFN responses, chemokines, and PRR signaling, were positively correlated with RBD IgG titer, neutralizing antibody titer, and CoV-2-specific memory B cell frequency. These were also positively correlated with activation of T and B cells, indicating the importance of coordination in acute infection for an optimal humoral response. Complement proteins were also enriched, consistent with prior studies showing complement can facilitate antigen retention in follicular DCs (Phan et al., 2007) and enhancing BCR-mediated signaling (Fischer et al., 1998; Lyubchenko et al., 2005). Plasmablasts were a positive correlate of antibodies and memory B cells, but it is unclear whether they play a functional role in clearing infection. Overall, these findings demonstrate that the immune response to acute infection is critical to an effective humoral response, emphasizing importance of coordination between innate and adaptive arms of immunity.

PASC or long COVID is one of the most enigmatic consequences of the ongoing pandemic. The involvement of many organ systems coupled with the highly subjective nature of symptoms has made it difficult to define consensus, objective criteria for diagnosis or clear therapeutic options. In our cohort, a subset of 3 COVID-19 participants progressed to PASC. All 3 PASC participants in our study were female, consistent with prior reports of female-biased presentation. Females are known to have stronger inflammatory responses in vaccines and infections, and predisposition to autoimmune disease, suggesting hyperinflammatory responses may be a risk factor for PASC (Klein and Flanagan, 2016). Significant correlation was observed between PASC and number of initial symptoms, as previously reported, but correlation with age was not reproduced, potentially due to our small sample size (Sudre et al., 2021).

Elevated inflammatory proteins in serum distinguished PASC participants from recovered COVID-19 participants. These signatures were coupled with evidence of persistent activation and inflammatory cytokine signaling in innate immune cells based on gene expression and chromatin accessibility after 30 days PSO. DCs and CD14 monocytes in PASC showed the most transcription factor motif enrichments. Among these, AP-1, STAT, IRF, BATF, and BACH suggest ongoing cellular stress, immune cell activation and differentiation, and inflammatory cytokine signaling during PASC. Gene expression signatures similarly showed stronger TNF signaling in CD14 monocytes from PASC participants. Early infection signaling and kinetics were also unique in PASC, including lower RLR and IFN responses in acute infection that did not wane longitudinally. This combination of changes mirrors severe COVID-19: dampened antiviral responses may fail to control viral replication in both, which can drive innate immune responses to persist beyond acute infection and cause ongoing pathology.

Integrative analysis identified multiple secreted proteins as potential therapeutic targets. Persistently elevated TNF may be an appealing target given the potential for TNF-driven pathogenic cell death and

correlations with disease severity and mortality (Del Valle et al., 2020; Karki et al., 2021). TNF can also drive IL-1β expression as well as AP-1 and STAT/IRF enrichment observed in motif analyses, motivating therapeutic targeting and blockade of these cytokines to potentially prevent the onset of PASC. LTA/TNFβ is a TNF family member and similarly upregulated in autoimmune diseases such as rheumatoid arthritis. Blockade in PASC may be beneficial and achieved by receptor antagonists (Browning, 2008) or TNF blockade (e.g., etanercept). Another promising target is IL-1β, which was significantly elevated in serum from PASC participants, coexpressed among pathways in CD14 monocytes by scRNAseq, and was both a predicted ligand signal and common downstream target of predicted ligand-receptor interactions. Both of these targets are consistent with risk factors observed in hyperinflammation from severe COVID-19, again suggesting similarities between severe disease and PASC. Broader anti-inflammatory therapy such as corticosteroids may be useful to attenuate pathogenic inflammation in PASC and has been tested in COVID-19 patients with persistent inflammatory lung disease (Myall et al., 2021). These novel insights into PASC can focus future studies on pathogenic mechanisms and therapeutic targets. Molecular classification disease heterogeneity in PASC may identify disease subsets to further enhance clinical management and optimize therapeutic strategies.

There are several key limitations to our study, including 1) a small sample size especially for PASC participants, 2) lack of geographic and racial diversity, 3) asynchronous sampling due to outpatient status, and 4) gaps in sampling during early infection (first ~7 days PSO) for some participants. Natural history studies are intrinsically limited to correlative associations. Confirming causality from our findings to mechanistically link early infection immune responses to convalescent CoV-2-specific immune responses will require preclinical models. Multi-omic assays were conducted on parallel samples and independently from CoV-2-specific assays, so relationships between different -omics and CoV-2 responses were inferred. Direct multiplexed analysis, particularly adding TCR and BCR clonality, will better enable dissection of virus-specific vs. non-specific immune mechanisms. Despite these weaknesses, our study provides insightful data that advance our understanding of SARS-CoV-2 infection, mild COVID-19, convalescence, and PASC.

Overall, our study results provide a comprehensive longitudinal roadmap of immune activation and resolution in mild COVID-19, including a potential mechanism for an age-dependent effect on immune responses. We observed a robust plasmablast response that may be tightly regulated by early IFN responses, and identified key early correlates of antibody and B cell responses, both findings which should be broadly tested as potential shared features in diverse natural infections. A subset of participants who progressed to PASC revealed novel inflammatory and non-inflammatory signatures in serum proteins, and innate immune-centric hyperactivation. Multiple potential therapeutic targets in PASC are nominated by our analyses, and serum protein biomarkers may provide objective diagnosis of inflammatory and non-inflammatory PASC after validation in larger cohorts. A more personalized approach to immunomonitoring and therapy will result in improved outcomes across the spectrum of COVID-19 and PASC.

Acknowledgements:

We thank the study participants for their dedication to this project; the Allen Institute founder, Paul G. Allen, for his vision, encouragement, and support; Ken Stuart, for constructive feedback on early drafts; the Human Immune System Explorer (HISE) software development team at the Allen Institute for Immunology for their support and dedication. This paper and the research behind it would not have been possible without the collaborative computational data analysis environment provided by HISE.

Funding:

The research reported in this publication was supported in part by COVID supplements from the National Institute of Allergy and Infectious Diseases and the Office of the Director of the National Institutes of Health under award numbers UM1AI068618-14S1 and UM1AI069481-14S1 (MJM); and ORIP/OD P51OD011132 (MSS). This work was also supported by Paul G. Allen Family Foundation Award #12931 (MJM); Seattle COVID-19 Cohort Study (Fred Hutchinson Cancer Research Center, MJM); the Joel D. Meyers Endowed Chair (MJM); An Emory EVPHA Synergy Fund award (MSS); COVID-Catalyst-I3 Funds from the Woodruff Health Sciences Center (MSS); the Center for Childhood Infections and Vaccines (MSS); Children's Healthcare of Atlanta (MSS), a Woodruff Health Sciences Center 2020 COVID-19 CURE Award (MSS) and the Vital Projects/Proteus funds. The content is solely the responsibility of the authors and does not necessarily represent the official views of the funders.

Figure legends:

Fig 1: Overview of the longitudinal mild COVID-19 cohort from acute infection through convalescence. **A)** Cohort overview and participant demographics. Eighteen participants had an initial blood draw within 15 days of developing symptoms (range 1-15 days) and were then followed longitudinally. **B)** Sample availability enumerated per assay type. PBMCs were analyzed by spectral flow cytometry, scRNAseq, scATACseq, and antigen-specific ICS assays. Serum was analyzed for SARS-CoV2 antibody serology or proteomics by Olink Explore 1536. Absent samples were due to limitations on material availability or timing. **C)** Longitudinal sampling timeline. PBMCs and serum were collected at 3-5 timepoints for each participant. Younger participants (top) are blue; older participants (bottom) are orange. Each Gantt is annotated with sex, documented comorbidities, and presentation of PASC. **D)** Self-reported symptoms occurring at any point during acute COVID-19 by subject. Illness severity score was calculated as described in Methods and shown vs. WHO ordinal severity. Each symbol represents one participant. Red symbols indicate PASC. **(E-G)** Cohort dynamics of SARS CoV2-specific adaptive immune responses: **E)** Aggregate frequencies of E, M, N, S, and ORF3, 6a, 7a, 7b, and 8-specific CD4+ and CD8+ T cells, **F)** titers of RBD IgG and neutralizing antibodies, and **G)** frequencies of S-specific plasmablasts and S-specific IgG+ memory B cells are shown over time for each donor with Loess smoothed curves overlaid with 95% confidence intervals shaded. Symbols for CD4+ and CD8+ T cell frequencies represent positive (filled) or negative (open) responses for each sample based on a positive response to any individual peptide pool stimulation determined using MIMOSA (Methods). **H)** Correlations between clinical metadata and estimates of SARS-CoV-2-specific immune responses. Day 30 estimates were used for all immune responses except neutralizing antibodies, which were estimated at day 42. Spearman's rank coefficients were calculated for each pairwise combination, multiple comparisons corrected by Benjamini-Hochberg, and only correlations with adjusted p-values < 0.05 are displayed. The size of symbols represents the magnitude of correlations.

Fig. 2: Early acute infection in mild COVID-19 is characterized by activation of T and B cells, and age-enhanced signatures of interferon signaling.
A) Volcano plot showing differential expression of serum proteins between COVID-19 participants at ≤ 15 days PSO (n=15) compared to uninfected controls (n=22). Significantly differential proteins are colored (FDR < 0.05). **B)** Flow cytometry analyses shows cell type proportion differences between COVID-19 participants (n=18) compared to uninfected controls (n=23). Parent populations are plotted as % of CD45+ PBMCs, while phenotypic markers are plotted as % of parent. Differential populations were determined by fitting a linear model with change in proportions as a function of infection status adjusted for age and sex. Only significant proportions with adjusted p-values < 0.05 for infection status are shown. **C)** GSEA performed on scRNAseq using differentially expressed genes from comparing older COVID-19 participants to younger COVID-19 in early acute infection within each cell type. Size of dots represents the percent of genes in each pathway that were enriched. Dot color represents the normalized enrichment score (NES) comparing older COVID-19 participants to younger COVID-19 participants. The top 10 most significant pathway enrichments are shown. **D)** Expression of genes enriched in IFN response pathways per cell type grouped by participant age and infection status. The column annotation bars represent the average gene expression across single cells per cell type and are scaled across samples. Gene expression was compared between groups using a wilcoxon rank sum test; asterisks indicate p < 0.05. **E)** Transcription factor motif analysis on scATACseq data showing differential accessibility of age-matched COVID-19 participants compared to uninfected controls in plasmablasts. Significantly enriched motifs were colored by motif family (Wilcoxon, FDR < 0.1), and the motifs with the largest shifts in each age subgroup (younger and older participants) are labeled. **F)** Predicted ligands signaling into plasmablasts during early acute infection. Ligand-receptor interaction analysis was performed using DEGs from scRNAseq as input for NicheNet. The top 10 predicted ligands are shown ranked by Pearson's correlation coefficient of target genes. Potential source cell types were identified from PBMCs cell types based on expression of the predicted ligands.

Fig. 3: Longitudinal analysis shows individual heterogeneity in path to convalescence with resolution of inflammatory cytokine signaling coordinated with increasing wound healing and EMT.
A) Heatmap of changes in serum proteins over time in mild COVID participants. Proteins that significantly changed over time were identified and enriched for pathways using Fisher's overlap test. Individual columns represent samples ordered by days PSO, with column annotations for days PSO and PASC (red) vs recovered (grey) provided. Rows represent individual proteins. Features were considered significant with adjusted p-values < 0.05. **B)** Heatmap of longitudinally changing cell frequencies quantified by flow cytometry among COVID-19 participants. Columns represent individual samples ordered by days PSO, with column annotations for days PSO and PASC (red) vs recovered (grey) provided. Rows represent significant cell frequencies shown as row-scaled % of total CD45+ cells or % of parent population. **C)** Pairwise correlations between functional pathways (circles, serum proteome) and cell frequencies (squares, flow cytometry; triangles, scRNAseq) over time. The antibody response memory B cells node constitutes plasmablasts (% of CD45+ cells), BCMA+, CD71+ and CD86+ (% of post-switch memory B cells) as determined by flow cytometry. The proliferating lymphocytes node constitutes CD4+, CD8+ and NK proliferating cells (% of PBMCs) as obtained by scRNAseq. The BAFF-R+ B cells node constitutes BAFF-R+ (% B cells) and BAFF-R+ (% of post-switch memory B cells). The edges to these specific nodes represent the average spearman correlation coefficient across these cell types to individual serum proteome features. Edges are colored by magnitude of positive (red) or negative (blue) Spearman correlation coefficients. Only significant correlations (adjusted p-values < 0.05) are shown. **D)** GSEA performed on scRNAseq genes that were longitudinally decreasing over time per participant by cell type. Dot size represents the percent of COVID-19 participants that showed enrichment for the indicated pathway and cell type. Dot color represents the negative NES indicating the magnitude of decreasing pathway expression over time. The top 10 significant pathway enrichments are shown. **E)** Longitudinal transcription factor motif accessibility for AP-1 in CD14+ monocytes from COVID-19 participants. AP-1 significantly decreased over time in most participants, but persisted in PASC participants (TEST, THRESHOLD). **F)** Principal coordinates analysis on all longitudinally changing proteins in COVID-19 participants was used to visualize heterogeneity in the path to convalescence. ***Inset***: early acute COVID-19 samples (***left***) and ~30 days PSO (***right***) were plotted with uninfected controls. The middle panel shows the progression of COVID-19 participants from early (black symbols) to late (red symbols) days PSO. Most COVID-19 participants (solid circle) were well separated from uninfected participants (green triangle) at the beginning but converged to the region of the latter as they recovered. The right panel shows the corresponding distances to the centroid of uninfected participants (solid black circles). The distances of uninfected participants were plotted with solid circles with randomly assigned days PSO between 0 and 5. The distances of recovered COVID-19 participants were plotted with black solid lines while those of PASC participants were plotted with red solid lines. Loess smoothing (blue line with 95% confidence intervals shaded grey) was used to guide the eye.

Fig. 4: Persistent immune activation distinguishes post-acute sequelae of SARS-CoV2 infection (PASC) from recovered COVID-19. A) Overview of symptom persistence for PASC participants. No PASC participants (n=3) had fully recovered at time of latest follow-up while all non-PASC participants (n=15) had recovered. **B)** SARS-CoV-2-specific adaptive immune responses estimated at day 30 or day 42 as indicated comparing PASC and recovered COVID-19 participants. Only estimates above the limit of detection are shown. **C)** Heatmap of differentially expressed serum proteins over time. Each protein's expression was fitted to a linear mixed-effects model. Only significantly differential proteins are shown with adjusted p-value < 0.05. **D)** scRNAseq SLEA pathway scores of significantly different pathways comparing PASC and recovered COVID-19 participant groups in early acute infection in CD14 monocytes. The SLEA pathway score was calculated per sample and tracked over time. Comparisons were significant for adjusted p-values < 0.05. **E)** Transcription factor motif analysis of scATACseq data in samples >30 days PSO. PASC participants were

compared to recovered COVID-19 participants and enrichments were calculated using ChromVar motif Z-scores. The top 50 largest significant motif differences are shown (Wilcoxon FDR <0.10). **F)** Ligand-receptor interaction analysis was used to identify predicted signals driving innate (CD14 monocyte) cells in PASC participants. The top 5 predicted ligands and their target gene signatures are shown. Ligands were ranked by Pearson correlation coefficient between expected and observed target gene expression.

Fig. 5: Immune correlates from early acute infection highlight the coordination of innate inflammatory response with humoral responses to SARS-CoV-2. Day 7 estimated serum proteins and pathway enrichments that significantly (spearman's correlation coefficients > 0.5 and adjusted p-values < 0.05) correlated with estimated day 30 RBD IgG titer (**A**) and day 42 neutralizing antibody titers (**B**). **C)** Venn diagram of the early acute protein feature overlaps that correlated with both day 30 RBD IgG and day 42 neutralizing antibody titers. Flow cytometry based cell proportions that significantly (spearman's correlation coefficients > 0.5 and adjusted p-values < 0.05) correlated with estimated day 30 RBD IgG titer (**D**) and day 42 neutralizing antibody titers (**E**). **F)** Venn diagram of the early acute cell proportion overlaps that correlated with both day 30 RBD IgG and day 42 neutralizing antibody titers.Rows correspond to proteins or cell frequencies measured by flow cytometry. Columns correspond to individual COVID-19 participants arranged by increasing order outcomes (represented as column annotation bars).

Fig. 6: Integrative analysis uncovers key nodes for immunomonitoring and potential therapeutic targets throughout infection, convalescence, and PASC. A) Differentially expressed immune-related proteins (n=75, p <0.05) observed in early acute infection (≤15 days PSO), longitudinally and in PASC COVID-19 subjects derived from serum proteomics study. **B)** Nichenet-based intercellular communication analyses of single cell RNA data from early acute COVID-19 infection subjects. We retrieved top 10 inferred ligands influencing the ligand-target expression in receiver cell types. The triangle shows the ligand and circle represents the receiver cell type. The edge between nodes and ligand shows the inferred relationship in early acute COVID-19 infection from scRNA data. The size of the triangle is proportional with the number of edges outgoing. **C)** The top 10 inferred ligands (per cell type) with the percent of cell types showing ligand activity, and **D)** the percentage of ligands activating downstream target genes in early acute COVID-19 infection were shown. **E)** The overlap between the inferred ligand-receptor interactions from differential intercellular communication between three subgroup comparisons: 1) early acute COVID-19 participants ≤ 15 days PSO compared to uninfected, 2) longitudinal COVID-19 at >15 days PSO compared to early acute COVID-19, and 3) PASC participants compared to recovered COVID-19 participants at all timepoints. Longitudinal changes in **F)** ligand and **G)** target usage in early acute COVID-19, longitudinal and PASC participants respectively are shown. Changes were calculated as the difference in predicted ligand per cell type **(F)** or downstream target genes regulated by predicted ligands **(G)** in the subgroup specified compared to respective control conditions listed above. Columns represent each subgroup and differences >10% were shown.

Supplemental figure legends:

Fig. S1: A) Principal component analysis (PCA) bi-plot of the serum proteome across all longitudinal COVID-19 participant samples (red points) and uninfected controls (green points). The loadings of the most varying proteins are represented by arrows; arrow length is proportional to the variance of the proteins contributing to sample distinction. Shapes of points represent sex and age represents age. **B)** PCA of flow cytometry cell frequencies across all longitudinal COVID-19 participant samples and uninfected controls, including batch bridging controls. Points are colored by batch ID. Principal Variant Component Analysis (PVCA) was performed as indicated in the bar plot to assess batch effects. The proportion of variance (y-axis) in cell frequencies contributed by each factor (x-axis) is depicted. **C)** PCA bi-plot of the flow cytometry based proportions across all longitudinal COVID-19 participant samples (red points) and uninfected controls (green points). The loading of the top varying cell proportions are represented by arrows. **D)** UMAP density representation per batch as grids and PVCA analysis (bar plot) of the scRNAseq batch bridging control samples. The proportion of variance (y-axis) in gene expression contributed by each factor (x-axis) is depicted in the bar plot. **E)** UMAP density representation per batch as grids and PVCA analysis (bar plot) of the full scRNAseq cohort samples including all COVID-19 longitudinal samples and uninfected controls. The proportion of variance (y-axis) in gene expression contributed by each factor (x-axis) is depicted in the bar plot. **F)** UMAP of the cell type annotation on scRNAseq data using the Weighted Nearest Neighbors (WNN) approach implemented in Seurat v4 with a CITE-seq based reference dataset (Hao et al., 2020b). Each point represents single cells color-coded by cell type label. **G)** Heatmaps of selected gene and predicted ADT (x-axes) expression by cell type (y-axes) of scRNAseq data. **H)** Correlation scatter plots between scRNA proportions (x-axis) and the equivalent population gating in flow cytometry (y-axis) across all samples. Significance of correlations was tested by a Spearman correlation test.

Fig. S2: A) Box and jitter plots of scRNAseq based cell type proportions that were significantly different (adjusted p-values < 0.05) comparing the early acute infection timepoints of COVID-19 participants (red) to uninfected controls (green) assessed by a fitting linear model adjusted for age and sex. **B)** Heatmap of the flow cytometry and scRNAseq cell type proportions (rows) that were significantly different (adjusted p-values < 0.05 assessed by wilcoxon rank sum test) comparing older to younger COVID-19 participants (columns) in early acute infection. **C)** Heatmap of serum proteins (rows) that were significantly different (adjusted p-values < 0.05 assessed by wilcoxon rank sum test) comparing older to younger COVID-19 participants (columns) in early acute infection. **D)** Bar plot of the number of DEGs (y-axis) comparing age-matched early acute COVID-19 participants to uninfected controls (per grid) within each cell type (x-axis) detected in scRNAseq. Number of DEGs that were significantly up-regulated (red) and down-regulated (blue) at an adjusted p-value < 0.05 are reported. **E)** GSEA pathway enrichment (y-axis) among DEGs comparing age matched early acute COVID-19 participants to uninfected controls (per grid) in every cell type (x-axis) of scRNAseq data. The color gradient of points represents the NES per pathway indicating up-regulation (red) or down-regulation (blue) of each pathway. The size of points represent the percent of genes enriched in a pathway per cell type and age group. **F)** GSEA pathway enrichment (y-axis) among DEGs comparing early acute infection timepoints of older COVID-19 participants to younger in every cell type (x-axis) of scRNAseq data. The color gradient of points represents the positive NES per pathway indicating up-regulation of the pathways in older participants. The size of points represent the percent of genes enriched in a pathway per cell type and age group. Pathways are arranged as being expressed in most to the least number of cell types. **G)** Scatterplot of the -log10 of the lowest P value per cell type by the absolute value of the maximum z-score shift per cell type. CD16 Monocytes, CD14 Monocytes, DCs, and plasmablasts appear to be the most impacted during the early infection period. **H)** Heatmap of top 50 motif accessibility changes during early COVID19 infection. Z-scores representing motif accessibility as compared to background were calculated for each cell. Z-score shifts were tested for statistical significance by a wilcoxon test with an FDR < 0.1. Only significant shifts are colored.

Fig. S3: A). Serum cytokines, chemokines and complement proteins (individual grids) among COVID-19 participants that significantly (adjusted p-values < 0.05) showed decrease over time. Individual lines are color coded by the participant ID. **B)** scRNA based cell type proportions (individual grids) among COVID-19 participants that significantly (adjusted p-values < 0.05) showed decrease over time. Individual lines are color coded by the participant ID. **C)** Pairwise correlations between functional pathways (circles, serum proteome) and cell type proportions (squares, flow cytometry; triangles, scRNAseq) overtime. The edge color gradient indicates significant (p-values < 0.05) positive (red) or negative (blue) spearman correlations over time. **D)** GSEA pathway enrichment (y-axis) among longitudinal gene changes per COVID-19 participant in every cell type (x-axis) of scRNAseq data. The size of points represents the percent of COVID-19 participants the pathway is enriched in. Pathways are arranged as being expressed in most to the least number of cell types across participants. **E)** Longitudinal IRF motif accessibility per participant over disease course. Curves are colored for PASC (red) and recovered (black) COVID-19 participants. Loess curves were added to visualize group trends. **F)** PCoA of serum proteome trajectories for individual COVID-19 participants and uninfected controls (black circles, no arrows). Symbols are colored by comorbidities and clinical features. Arrows are colored by visit interval over time.

Fig. S4: A) Number of differentially expressed serum proteins over time compared to uninfected controls for each COVID-19 participant. Outlier analysis was performed comparing COVID-19 participants to uninfected background and selecting features >2 standard deviations from the mean. **B)** Differential serum proteome features (130, p<0.05) between the PASC subjects and recovered COVID19+ subjects using linear mixed model adjusted for age, sex.**C)** Bar plot of the number of DEGs (y-axis) comparing early acute infection timepoints of PASC participants to recovered COVID-19 participants in every cell type (x-axis) detected in scRNAseq. Number of DEGs that were significantly up-regulated (red) and down-regulated (blue) at an adjusted p-value < 0.05 are reported. **D)** Box plot of the SLEA score (y-axis) of TNF signaling via NFkb and Hypoxia pathways significantly upregulated (adjusted p-values < 0.05) in CD8 TEMs from PASC compared to recovered COVID-19 participants in early acute infection. The SLEA score of the pathways per sample was calculated based on scRNAseq gene expression per cell type and tracked over the course of disease (x-axis). **E)** Arc co-expression network of genes enriched in the TNF signaling pathway in CD14 monocytes, from early acute timepoints of PASC participants. Edges represent correlation between genes at greater than 0.8 spearman correlation coefficient, while size of each gene node represents the degree or number of gene correlations above mentioned coefficient. **F)** Box plot of the SLEA score (y-axis) of the RIG-I receptor signaling and interferon response scRNA pathways significantly downregulated (adjusted p-values < 0.05) in CD14 monocytes, CD16 monocytes and CD8 TEM from PASC compared to recovered COVID-19 participants in early acute infection. The SLEA score of the pathways per sample was calculated and tracked over the course of disease (x-axis). **G)** Arc co-expression network of genes enriched in the RIG-I and interferon responses in CD14 monocytes, from early acute timepoints of PASC participants. Edges represent correlation between genes at greater than 0.8 spearman correlation coefficient, while size of each gene node represents the degree or number of gene correlations above mentioned coefficient. **H)** Ligand activity observed in CD14 monocytes and their log-fold change in sender cell types in PASC subjects **(I)**. **J)** Target genes of predicted ligands to CD14 monocytes include *IL1B*, *FOS*, *NAMPT*, *BCL2A1*, *PLAUR*, and *HIF1A*.

Fig. S5. A) Correlation scatterplots between the observed (y-axis) and estimated values (x-axis) as obtained by fitting linear mixed effect models over time to the serum proteome and **B)** to flow cytometry based proportions. For flow cytometry, the top 15 (ranked by spearman's correlation coefficient) are shown. All correlations were significant (p-values < 0.05) with greater than a 0.5 coefficient as assessed by the Spearman's correlation test. **C)** Day 7 estimated serum proteins and pathway enrichments, and cell proportions **(D)** that significantly correlated (spearman's correlation coefficients > 0.5 and adjusted p-values < 0.05) with the estimated S-specific memory B cells. Rows correspond to proteins or cell frequencies measured

by flow cytometry. Columns correspond to individual COVID-19 participants arranged by increasing order outcomes (represented as column annotation bars).

Fig. S6. A) Gene expression of differentially expressed serum proteins per cell type. The scaled average expression shown for each gene in a given cell type in COVID19 participants. The size of the circle represents the percent (per number of cells) expression observed. **B)** Cell-cell communication analysis comparison between early visit and PASC subjects with control as healthy and non-PASC/recovered COID19 subjects respectively. Pearson correlation coefficient (PCC) between a ligand's target predictions and the observed transcriptional response were calculated and corresponding scores attributed to ligand-receptors were visualized in scatter plot. **C)** Serum protein expression changes in COVID-19 participants (recovered and PASC) are shown in the box plot. Samples were grouped based on days PSO covering: 1) early acute infection ≤15 days; 2) late acute infection, 16-30 days; and 3) post-acute infection and convalescence, ≥31 days. T-tests were used to compare the PASC to recovered participants, and a representative subset of significantly differential proteins is shown. P-values < 0.05 were considered statistically significant.

METHODS

RESOURCE AVAILABILITY

Lead contacts

Further information and requests for resources and reagents should be directed to and will be fulfilled by the lead contacts: Gregory Szeto (greg.szeto@alleninstitute.org); M. Juliana McElrath (jmcelrat@fredhutch.org); and Thomas F. Bumol (tomb@alleninstitute.org).

Materials Availability:

This study did not generate new unique reagents.

Data and code availability

The RNAseq and ATACseq data generated during this study are available at GEO under accession number GSE173590. All analytical code and figure generation will be available on Github.

EXPERIMENTAL MODEL AND SUBJECT DETAILS

Demographics

Eighteen immunocompetent study participants who were diagnosed with SARS-CoV-2 were selected for these studies, as they had donated at least one sample of serum at or earlier than 15 days post-symptom onset. Both studies were recruited at the Seattle Vaccine Trials Unit (Seattle, Washington, USA). The cohort demographics are described in the following table.

Volunteers with SARS CoV-2 Diagnosis	Females	Males
Number	10	8
Age	Mean 46 Range 29-79	Mean 46 Range 22-65
Race and Ethnicity	100% White (n=10)	100% White (n=8) 12.5% Hispanic/Latino (n=1)
Co-morbidities previous to SARS-CoV2 Diagnosis	Asthma (n=1) High Blood Pressure (n=1) Autoimmune Disease (n=2) Current or past Smoker (n=1) Anemia (n=1) Obesity (n=2)	Heart disease (n=1) High Blood Pressure (n=1) Current or past Smoker (n=1) Obesity (n=1)

Uninfected SARS-CoV-2-negative Volunteers	Females	Males
Number	10	13
Age	Mean 47 Range 29-61	Mean 48 Range 31-77
Race and Ethnicity	100% White (n=10)	84.6% White (n=11) 15.4% Hispanic/Latino (n=2) Other: American Indian or Alaska Native;White (n=1) Asian;White (n=1)
Co-morbidities previous to SARS-CoV2 Diagnosis	Asthma (n=1) High Blood Pressure (n=1) Autoimmune Disease (n=3) Current or past Smoker (n=3) Anemia (n=1)	COPD (n=1) Cancer (n=1) Current or past Smoker (n=2) High Blood Pressure (n=1) Hypertension(n=1)

Informed consent was obtained from all participants and the Fred Hutchinson Cancer Research Center Institutional Review Board approved the study and procedures (IR10440).

METHODS DETAILS

Study Conduct

Peripheral blood mononuclear cells (PBMCs) and serum were collected from participants enrolled in the longitudinal study, “Seattle COVID-19 Cohort Study to Evaluate Immune Responses in Persons at Risk and with SARS-CoV-2 Infection”. Eligibility criteria included adults in the greater Seattle area at risk for SARS-CoV2 infection or those diagnosed with COVID-19 by a commercially available SARS CoV-2 PCR assay. Study data were collected and managed using REDCap electronic data capture tools hosted at Fred Hutchinson Cancer Research Center, including detailed information on symptoms during acute infection and longitudinal follow-up ranging from 33-233 days post symptom onset. Plasma from pre-pandemic controls used for ELISA controls were blindly selected at random from the study, “Establishing Immunologic Assays for Determining HIV-1 Prevention and Control”, with no considerations made for age, or sex. Informed consent was obtained from all participants at the Seattle Vaccine Trials Unit and the Fred Hutchinson Cancer Research Center Institutional Review Board approved the studies and procedures.

Regulatory approvals from FH and AIFI

COVID19 FH samples and healthy controls: FH RG: 1007696 IR File: 10440 Main Consent 04/05/2020 and 6/04/2020 Seattle COVID-19 Cohort Study to Evaluate Immune Responses in Persons at Risk and with SARS-

CoV-2 Infection. IR File: 5567 Main Consent 08/04/2017 Establishing Immunologic Assays for Determining HIV-1 Prevention and Control.
Batch control leukopack from BIOIVT used in flow cytometry: PROSPECTIVE COLLECTION OF NON-MOBILIZED LEUKOCYTES VIA LEUKAPHERESIS FOR RESEARCH; PROTOCOL NO: SERATRIALS-18002; WIRB® Protocol #20190318

Serum and PBMC isolation

Blood collected in SST tubes was allowed to clot for at least 30 min at room temperature. Following cotting, the samples were centrifuged in the primary tubes at 1600-1800 X for 10 min. Serum was transferred to a 15ml tube, aliquoted into 300ul aliquots and stored at -80°C until use in the assays.

Blood collected in acid citrate dextrose tubes was transferred to Leucosep tubes (Greiner Bio One). The tube was centrifuged at 800-1000g for 15 min and the PBMC layer recovered above the frit. Peripheral blood mononuclear cells (PBMCs) were washed twice with Hanks Balanced Solution without Ca+ or Mg+ (Gibco) at 200-400xg for 10 min, counted, and aliquoted in heat-inactivated fetal bovine serum with 10% dimethylsulfoxide (DMSO, Sigma) for cryopreservation. PBMCs were cryopreserved at -80°C in Stratacooler (Nalgene) and transferred to liquid nitrogen for long-term storage.

Cell Type Flow Cytometry

To assess cell type proportions, PBMCs were analyzed with four 25-color immunophenotyping flow cytometry panels (P1, P2, P3 and P4). 1×10^6 thawed PBMCs were centrifuged (750×g for 5 minutes at 4°C) using a swinging bucket rotor (Beckman Coulter Avanti J-15RIVD with JS4.750 swinging bucket, B99516), the supernatant was removed using a vacuum aspirator pipette, and the cell pellet resuspended in DPBS without calcium and magnesium (Corning 21-031-CM). Cells were incubated with Fixable Viability Stain 510 (BD, 564406) and an Fc receptor blocking reagent, TruStain FcX (BioLegend, 422302) P1, P3 and P4 or purified mouse IgG (Bio-Rad, PMP01) P2 for 30 minutes at 4°C, then washed with chilled Cell Staining Buffer (BioLegend, 420201). Cells were stained with a cocktail of antibodies (P1, P2, P3 and P4) in Cell Staining Buffer plus BD Horizon Brilliant Stain Buffer Plus (BD, 566385) (**Key Resources Table**) at a staining volume of 100 µl for 30 minutes at 4°C, then washed with chilled Cell Staining Buffer. Fixation was performed by resuspending cells in 100 µl of FluoroFix Buffer (BioLegend, 422101) and incubating for 30 minutes at 25°C, protected from light. Following fixation, cells were washed twice with Cell Staining Buffer and resuspended in 100 µl Cell Staining Buffer. Stained cells were analyzed on a 5 laser Cytek Aurora spectral flow cytometer. Spectral unmixing was calculated with pre-recorded reference controls using Cytek SpectroFlo software (Version 2.0.2). Cell types were quantified by traditional bivariate gating analysis performed with FlowJo cytometry software (Version 10.7)

Spike and RBD Memory B cell flow cytometry assays

Fluorescent SARS-CoV-2-specific S6P (Hsieh et al., 2020) (provided by Roland Strong, Fred Hutchinson Cancer Research Center, Seattle, WA) and RBD (provided by Leonidas Stamatatos, Fred Hutchinson Cancer Research Center, Seattle, WA) probes were made by combining biotinylated protein with fluorescently labeled streptavidin (SA). The S6P probes were made at a ratio of 1:1 molar ratio of trimer to SA. Two S6P probes, one labeled with AlexaFluor488 (Invitrogen), one labeled with AlexaFluor647 (Invitrogen), were used in this panel in order to increase specificity of the detection of SARS-CoV-2-specific B cells. The RBD probe was prepared at a 4:1 molar ratio of RBD monomers to SA, labeled with R-phycoerythrin (Invitrogen). Cryopreserved PBMCs from SARS-CoV-2-convalescent participants and a pre-pandemic SARSCoV-2-naïve donor were thawed at 37°C and stained for SARS-CoV-2-specific memory B cells as described previously (Seydoux et al., 2020) with a flow cytometry panel shown in Reagents Table 1. Cells were stained first with the

viability stain (Invitrogen) in PBS for 15 min at 4°C. Cells were then washed with 2% FBS/PBS and stained with a cocktail of the three probes for 30 min at 4°C. The probe cocktail was washed off with 2% FBS/PBS and the samples were stained with the remaining antibody panel and incubated for 25 min at 4°C. The cells were washed two times and resuspended in 1% paraformaldehyde/1x PBS for collection on a LSR II or FACSymphony flow cytometer (BD Biosciences). Data was analyzed in Flow Jo version 9.9.4.

Intracellular Cytokine Staining (ICS) Assay

Flow cytometry was used to examine SARS-CoV-2-specific CD4+ and CD8+ T-cell responses using a validated ICS assay. The assay was similar to a published report (Dintwe et al., 2019; Horton et al., 2007) and the details of the staining panel are included in Reagents Table 2. Peptide pools covering the structural proteins of SARS-CoV-2 were used for the six-hour stimulation. Peptides matching the SARS-CoV-2 spike sequence (316 peptides, plus 4 peptides covering the G614 variant) were synthesized as 15 amino acids long with 11 amino acids overlap and pooled in 2 pools (S1 and S2) for testing (BioSynthesis). All other peptides were 13 amino acids overlapping by 11 amino acids and were synthesized by GenScript. The peptides covering the envelope (E), membrane (M) and nucleocapsid (N) were initially combined into one peptide pool, but the majority of the assays were performed using a separate pool for N and one that combined only E and M. Several of the open reading frame (ORF) peptides were combined into two pools, ORF 3a and 6, and ORF 7a, 7b and 8. All peptide pools were used at a final concentration of 1 microgram/ml for each peptide. As a negative control, cells were not stimulated, only the peptide diluent (DMSO) was included. As a positive control, cells were stimulated with a polyclonal stimulant, staphylococcal enterotoxin B (SEB). Cells expressing IFNγ and/or IL-2 and/or CD154 were the primary immunogenicity endpoint for CD4 T cells and cells expressing IFNγ were the primary immunogenicity endpoint for CD8 T cells. The overall response to SARS-CoV-2 was defined as the sum of the background-subtracted responses to each of the individual pools. A sample was considered positive for CD4+ or CD8+ T cell responses to SARS-CoV-2 if any of the CD4+ or CD8+ T cell responses to the individual peptide pool stimulations was positive. Positive responses to a given peptide pool stimulation were determined using the MIMOSA (Mixture Models for Single-Cell Assays) method (Finak et al. 2014). The MIMOSA method uses Bayesian hierarchical mixture models that incorporate information on cell count and cell proportion to define a positive response by comparing peptide-stimulated cells and unstimulated negative controls. MIMOSA estimates the probabilities that peptide-stimulated responses are responders and applies a false-discovery rate multiplicity adjustment procedure (Newton et al 2004). Responses with false-discovery rate q-values < 0.05 were considered positive.The total number of CD4+ T cells must have exceeded 10,000 and the total number of CD8 T cells must have exceeded 5,000 for the assay data to be included in the analysis.

Antibody ELISAs for RBD and N

Half-well area plates (Greiner) were coated with purified RBD protein at 16.25ng/well in PBS (Gibco) for 14-24h at room temperature. After 4 150ul washes with 1X PBS, 0.02% Tween-2 (Sigma) using the BioTek ELx405 plate washer, the IgA and IgG plates were blocked at 37°C for 1-2 hours with 1X PBS, 10% non-fat milk (Lab Scientific), 0.02% Tween-20 (Sigma); IgM plates were blocked with 1X PBS, 10% non-fat milk, 0.05% Tween-20.

Serum samples were heat inactivated by incubating at 56°C for 30 minutes, then centrifuged at 10,000 x g / 5 minutes, and stored at 4°C previous to use in the assay. For IgG ELISAs, serum was diluted into blocking buffer in 7-12 1:4 serial dilutions starting at 1:50. For IgM and IgA ELISAs, serum was diluted into 7 1:4 serial dilutions starting at 1:12.5 to account for their lower concentration. A qualified pre-pandemic sample (negative control) and a standardized mix of seropositive serums (positive control) was run in each plate and using to define passing criteria for each plate. All controls and test serums at multiple dilutions were plated in duplicate

and incubated at 37°C for 1 hour, followed by 4 washes in the automated washer. 8 wells in each plate did not receive any serum and served as blocking controls.

Plates then were plated with secondary antibodies (all from Jackson ImmunoResearch) diluted in blocking buffer for 1h at 37C. IgG plates used donkey anti-human IgG HRP diluted at 1:7500; IgM plates used goat anti-human IgM HRP diluted at 1:10,000; IgA plates used goat anti-human IgA HRP at 1:5000. After 4 washes, plates were developed with 25ul of SureBlock Reserve TMB Microwell Peroxide Substrate (Seracare) for 4 min, and the reaction stopped by the addition of 50ml 1N sulfuric acid (Fisher) to all wells. Plates were read at OD_{450nm} on SpectraMax i3X ELISA plate reader within 20 min of adding the stop solution.

OD_{450nm} measurements for each dilution of each sample were used to extrapolate RBD endpoint titers when CVs were less than 20%. Using Excel, endpoint titers were determined by calculating the point in the curve at which the dilution of the sample surpassed that of 5 times the average OD_{450nm} of blocking controls + 1 standard deviation of blocking controls.

N IgG was measured using SARS CoV-2 IgG Architect (Abbot), and index values used as a quantitative measure of the N binding activity.

Neutralizing antibody assay

Viruses and cells

VeroE6 cells were obtained from ATCC (clone E6, ATCC, #CRL-1586) and cultured in complete DMEM medium consisting of 1x DMEM (VWR, #45000-304), 10% FBS, 25mM HEPES Buffer (Corning Cellgro), 2mM L-glutamine, 1mM sodium pyruvate, 1x Non-essential Amino Acids, and 1x antibiotics. The infectious clone SARS-CoV-2 (icSARS-CoV-2-mNG), derived from the 2019-nCoV/USA_WA1/2020 strain, was propagated in VeroE6 cells (ATCC) and sequenced (Xie et al. 2020).

Focus Reduction Neutralization Test

Neutralization assays with SARS-CoV-2 virus were performed as previously described (Vanderheiden et al. 2020). Plasma/serum were serially diluted (three-fold) in serum-free Dulbecco's modified Eagle's medium (DMEM) in duplicate wells and incubated with 100–200 FFU infectious clone derived SARS-CoV-2-mNG virus at 37°C for 1 hr. The antibody-virus mixture was added to VeroE6 cell (C1008, ATCC, #CRL-1586) monolayers seeded in 96-well blackout plates and incubated at 37°C for 1 h. Post-incubation, the inoculum was removed and replaced with pre-warmed complete DMEM containing 0.85% methylcellulose. Plates were incubated at 37°C for 24 h. After 24 h, methylcellulose overlay was removed, cells were washed twice with PBS and fixed with 2% paraformaldehyde in PBS for 30 min at room temperature. Following fixation, plates were washed twice with PBS and foci were visualized on a fluorescence ELISPOT reader (CTL ImmunoSpot S6 Universal Analyzer) and enumerated using Viridot (Katzelnick et al. 2018). The neutralization titers were calculated as follows: 1 - (ratio of the mean number of foci in the presence of sera and foci at the highest dilution of respective sera sample). Each specimen was tested in two independent assays performed at different times. The FRNT-mNG_{50} titers were interpolated using a 4-parameter nonlinear regression in GraphPad Prism 8.4.3. Samples with an FRNT-mNG_{50} value that was below the limit of detection were plotted at 20.

Single-cell RNA-seq

Sample preparation, hashing, and pooling: Single-cell RNA-seq libraries were generated using the 10x Genomics Chromium 3' Single Cell Gene Expression assay (#1000121) and Chromium Controller Instrument

according to the manufacturer's published protocol with modifications for cell hashing (Stoeckius et al., 2018). To block off-target antibody binding, Blocking Solution (5 µL of Human Trustain FcX (BioLegend #422302) , and13.7 µL of a 10% Bovine Serum Albumin (BSA)) was added to 500,000 cells suspended in 50 µL Dulbecco's Phosphate Buffered Saline (DPBS; Corning Life Sciences #21-031-CM) and incubated for 10 minutes on ice. To stain samples, 0.5 µg (1 µL) of a TotalSeq™-A anti-human Hashtag Antibody was suspended in 31.3 µL DPBS/2% BSA, then added to each sample with . For each batch of samples, 100,000 cells from 8 hashedsamples with a distinct Hashtag Antibody were pooled into Pool 1; 8 additional samples were pooled using the same method into Pool 2. Roughly 20,000 cells from a Leukopak healthy control were also labeled with a distinct TotalSeq™-A Hashtag Antibody, and were spiked into each pool to serve as a batch control.

Droplet encapsulation and reverse transcription: From each pool, 64,000 cells were loaded into each well of a Chromium Single Cell Chip G (10x Genomics #**1000073**) (8 wells per chip), targeting a recovery of 20,000 singlets from each well. Gel Beads-in-emulsion (GEMs) were then generated using the 10x Chromium Controller. The resulting GEM generation products were then transferred to semi-skirted 96-well plates and reverse transcribed on a C1000 Touch Thermal Cycler programmed at 53°C for 45 minutes, 85°C for 5 minutes, and a hold at 4°C. Following reverse transcription, GEMs were broken and the pooled single-stranded cDNA and Hashtag Oligo fractions were recovered using Silane magnetic beads (Dynabeads MyOne SILANE #37002D).

Library generation and separation: Barcoded, full-length cDNA including the Hashtag Oligos (HTOs) from the TotalSeq™-A Hashtag Antibodies were then amplified with a C1000 Touch Thermal Cycler programmed at 98°C for 3 minutes, 11 cycles of (98°C for 15 seconds, 63°C for 20 seconds, 72°C for 1 minute), 72°C for 1 minute, and a hold at 4°C. Amplified cDNA was purified and separated from amplified HTOs using a 0.6x size selection via SPRIselect magnetic bead (Beckman Coulter #22667) and a 1:10 dilution of the resulting cDNA was run on a Fragment Analyzer (Agilent Technologies #**5067-4626**) to assess cDNA quality and yield. HTO libraries were purified further with SPRIselect magnetic bead (Beckman Coulter #22667) and amplified and indexed with a custom HTO i7 index on a C1000 Touch Thermal Cycler programmed at 95°C for 3 minutes, 10 cycles of (95°C for 20 seconds, 64°C for 30 seconds, 72°C for 20 seconds), 72°C for 1 minute, and a hold at 4°C. The resulting HTO libraries were purified with SPRIselect magnetic bead (Beckman Coulter #22667) post-amplification and a 1:10 dilution of the resulting HTO libraries were run on a Fragment Analyzer (Agilent Technologies #**5067-4626**) to assess HTO quality and yield. A quarter of the cDNA sample (10 ul) was used as input for library preparation. Amplified cDNA was fragmented, end-repaired, and A-tailed is a single incubation protocol on a C1000 Touch Thermal Cycler programmed at 4°C start, 32°C for minutes, 65°C for 30 minutes, and a 4°C hold. Fragmented and A-tailed cDNA was purified by performing a dual-sided size-selection using SPRIselect magnetic beads (Beckman Coulter #22667). A partial TruSeq Read 2 primer sequence was ligated to the fragmented and A-tailed end of cDNA molecules via an incubation of 20°C for 15 minutes on a C1000 Touch Thermal Cycler. The ligation reaction was then cleaned using SPRIselect magnetic beads (Beckman Coulter #22667). PCR was then performed to amplify the library and add the P5 and indexed P7 ends (10x Genomics #1000084) on a C1000 Touch Thermal Cycler programmed at 98°C for 45 seconds, 13 cycles of (98°C for 20 seconds, 54°C for 30 seconds, 72°C for 20 seconds), 72°C for 1 minute, and a hold at 4°C. PCR products were purified by performing a dual-sided size-selection using SPRIselect magnetic beads (Beckman Coulter #22667) to produce final, sequencing-ready libraries.

Quantification and sequencing: Final libraries were quantified using Picogreen and their quality was assessed via capillary electrophoresis using the Agilent Fragment Analyzer HS DNA fragment kit and/or Agilent Bioanalyzer High Sensitivity chips. Libraries were sequenced on the Illumina NovaSeq platform using S4 flow cells. Read lengths were 28bp read1, 8bp i7 index read, 91bp read2.

Single-cell ATAC-seq

FACS neutrophil depletion: To remove dead cells, debris, and neutrophils prior to scATAC-seq as described previously (Swanson et al. 2021), PBMC samples were sorted by fluorescence activated cell sorting (FACS) prior to cell permeabilization. Cells were incubated with Fixable Viability Stain 510 (BD, 564406) for 15 minutes at room temperature and washed with AIM V medium (Gibco, 12055091) plus 25 mM HEPES before incubating with TruStain FcX (BioLegend, 422302) for 5 minutes on ice, followed by staining with mouse anti-human CD45 FITC (BioLegend, 304038) and mouse anti-human CD15 PE (BD, 562371) antibodies for 20 minutes on ice. Cells were washed with AIM V medium plus 25 mM HEPES and sorted on a BD FACSAria Fusion. A standard viable CD45+ cell gating scheme was employed; FSC-A x SSC-A (to exclude sub-cellular debris), two FSC-A doublet exclusion gates (FSC-W followed by FSC-H), dead cell exclusion gate (BV510 LIVE/DEAD negative), followed by CD45+ inclusion gate. Neutrophils (defined as SSC^{high}, $CD15^{+}$) were then excluded in the final sort gate. An aliquot of each post-sort population was used to collect 50,000 events to assess post-sort purity.

Sample preparation: Permeabilized-cell scATAC-seq was performed as described previously (Swanson et al. 2021). A 5% w/v digitonin stock was prepared by diluting powdered digitonin (MP Biomedicals, 0215948082) in DMSO (Fisher Scientific, D12345), which was stored in 20 µL aliquots at −20°C until use. To permeabilize, 1×10^{6} cells were added to a 1.5 mL low binding tube (Eppendorf, 022431021) and centrifuged (400×g for 5 min at 4°C) using a swinging bucket rotor (Beckman Coulter Avanti J-15RIVD with JS4.750 swinging bucket, B99516). Cells were resuspended in 100 µL cold isotonic Permeabilization Buffer (20 mM Tris-HCl pH 7.4, 150 mM NaCl, 3 mM MgCl2, 0.01% digitonin) by pipette-mixing 10 times, then incubated on ice for 5 min, after which they were diluted with 1 mL of isotonic Wash Buffer (20 mM Tris-HCl pH 7.4, 150 mM NaCl, 3 mM MgCl2) by pipette-mixing five times. Cells were centrifuged (400×g for 5 min at 4°C) using a swinging bucket rotor, and the supernatant was slowly removed using a vacuum aspirator pipette. Cells were resuspended in chilled TD1 buffer (Illumina, 15027866) by pipette-mixing to a target concentration of 2,300-10,000 cells per µL. Cells were filtered through 35 µm Falcon Cell Strainers (Corning, 352235) before counting on a Cellometer Spectrum Cell Counter (Nexcelom) using ViaStain acridine orange/propidium iodide solution (Nexcelom, C52-0106-5).

Tagmentation and fragment capture: scATAC-seq libraries were prepared according to the Chromium Single Cell ATAC v1.1 Reagent Kits User Guide (CG000209 Rev B) with several modifications. 15,000 cells were loaded into each tagmentation reaction. Permeabilized cells were brought up to a volume of 9 µl in TD1 buffer (Illumina, 15027866) and mixed with 6 µl of Illumina TDE1 Tn5 transposase (Illumina, 15027916). Transposition was performed by incubating the prepared reactions on a C1000 Touch thermal cycler with 96–Deep Well Reaction Module (Bio-Rad, 1851197) at 37°C for 60 minutes, followed by a brief hold at 4°C. A Chromium NextGEM Chip H (10x Genomics, 2000180) was placed in a Chromium Next GEM Secondary Holder (10x Genomics, 3000332) and 50% Glycerol (Teknova, G1798) was dispensed into all unused wells. A master mix composed of Barcoding Reagent B (10x Genomics, 2000194), Reducing Agent B (10x Genomics, 2000087), and Barcoding Enzyme (10x Genomics, 2000125) was then added to each sample well, pipette-mixed, and loaded into row 1 of the chip. Chromium Single Cell ATAC Gel Beads v1.1 (10x Genomics, 2000210) were vortexed for 30 seconds and loaded into row 2 of the chip, along with Partitioning Oil (10x Genomics, 2000190) in row 3. A 10x Gasket (10x Genomics, 370017) was placed over the chip and attached to the Secondary Holder. The chip was loaded into a Chromium Single Cell Controller instrument (10x Genomics, 120270) for GEM generation. At the completion of the run, GEMs were collected and linear amplification was performed on a C1000 Touch thermal cycler with 96–Deep Well Reaction Module: 72°C for 5 min, 98°C for 30 sec, 12 cycles of: 98°C for 10 sec, 59°C for 30 sec and 72°C for 1 min.

Sequencing library preparation: GEMs were separated into a biphasic mixture through addition of Recovery Agent (10x Genomics, 220016), the aqueous phase was retained and removed of barcoding reagents using Dynabead MyOne SILANE (10x Genomics, 2000048) and SPRIselect reagent (Beckman Coulter, B23318) bead clean-ups. Sequencing libraries were constructed by amplifying the barcoded ATAC fragments in a sample indexing PCR consisting of SI-PCR Primer B (10x Genomics, 2000128), Amp Mix (10x Genomics, 2000047) and Chromium i7 Sample Index Plate N, Set A (10x Genomics, 3000262) as described in the 10x scATAC User Guide. Amplification was performed in a C1000 Touch thermal cycler with 96–Deep Well Reaction Module: 98°C for 45 sec, for 9 to 11 cycles of: 98°C for 20 sec, 67°C for 30 sec, 72°C for 20 sec, with a final extension of 72°C for 1 min. Final libraries were prepared using a dual-sided SPRIselect size-selection cleanup. SPRIselect beads were mixed with completed PCR reactions at a ratio of 0.4x bead:sample and incubated at room temperature to bind large DNA fragments. Reactions were incubated on a magnet, the supernatant was transferred and mixed with additional SPRIselect reagent to a final ratio of 1.2x bead:sample (ratio includes first SPRI addition) and incubated at room temperature to bind ATAC fragments. Reactions were incubated on a magnet, the supernatant containing unbound PCR primers and reagents was discarded, and DNA bound SPRI beads were washed twice with 80% v/v ethanol. SPRI beads were resuspended in Buffer EB (Qiagen, 1014609), incubated on a magnet, and the supernatant was transferred resulting in final, sequencing-ready libraries.

Quantification and sequencing: Final libraries were quantified using a Quant-iT PicoGreen dsDNA Assay Kit (Thermo Fisher Scientific, P7589) on a SpectraMax iD3 (Molecular Devices). Library quality and average fragment size was assessed using a Bioanalyzer (Agilent, G2939A) High Sensitivity DNA chip (Agilent, 5067-4626). Libraries were sequenced on the Illumina NovaSeq platform with the following read lengths: 51nt read 1, 8nt i7 index, 16nt i5 index, 51nt read 2.

Olink serum protein measurement

Serum samples were inactivated with 1% Triton X-100 for 2h at room temperature according to the Olink COVID-19 inactivation protocol. Inactivated samples were then run on the Olink Explore 1536 platform, which uses paired antibody proximity extension assays (PEA) and a next generation sequencing (NGS) readout to measure the relative expression of 1472 protein analytes per sample. Analytes from the inflammation, oncology, cardiometabolic, and neurology panels were measured.

For plate setup, samples were randomized across plates to achieve a balanced distribution of age and gender. Longitudinal samples from the same patient were run on the same plate. To facilitate comparisons with future batches, sera from 15 donors was commercially purchased (BioIVT) and randomly interspersed amongst the above study samples. Commercial samples included serum from COVID-19 serology-negative, serology-positive, PCR-positive, and recovered (no longer symptomatic) donors.

Data were first normalized to an extension control that was included in each sample well. Plates were then standardized by normalizing to inter-plate controls run in triplicate on each plate. Data were then intensity normalized across all samples. Final normalized relative protein quantities were reported as log2 normalized protein expression (NPX) values.

Data analyses

Illness severity metrics and scoring

For acute COVID-19, categorization of illness severity was classified by participant report of impact on Activities of Daily Living (ADLs) for each day of illness (of Health et al. 2017). Severe days hospitalized were also recorded as were any treatment or therapies received. Participants were scored according to their maximum severity for each day: 0, no symptoms; 1, mild impact on ADLs reported; 2, moderate impact on ADLs reported; 3, severe illness without hospitalization; 4, severe illness with hospitalization; 5, life threatening illness hospitalized with ICU care. Durations were assigned for days spent at each illness severity. A cumulative illness severity score was calculated for each patient by multiplying each severity score by the number of days spent at each level, then summing all values. Participants were classified as post-acute sequelae of SARS-CoV-2 infection (PASC) if any symptoms continued from acute illness or related to COVID-19 beyond 60 days.

Metadata correlations

Spearman's rank correlation coefficients were calculated for pairwise combinations of SARS-CoV-2-specific immune response estimates and clinical metadata. Symptoms at diagnosis and comorbidities with ≤ 3 events were excluded from analysis. P-values were adjusted using Benjamini-Hochberg method and adjusted p-values ≤ 0.05 were considered significant.

Flow cytometry

Following sample acquisition on the Cytek Aurora flow cytometer, samples were unmixed using library reference controls pre-recorded on the instrument using the batch control sample, and the data files were exported in FCS 3.1 format. Unmixing performance was visually checked and unmixing errors were adjusted with compensation on the batch control sample in each individual batch using FlowJo v10.7.1. Compensation adjustments from the batch control were applied to the entire batch. The fluorescent channels in each compensated FCS file were transformed using the logicle transform. The compensated and transformed data was analyzed using bivariate hierarchical gating. Initial placement of gates was implemented automatically using the openCyto R package using customized gating templates for each panel. Following the preliminary automated gate placement, all gates were visually checked for errors and corrected manually per sample in a Flowjo v10.7.1 workspace file generated with the CytoML R package (Finak, Jiang, and Gottardo 2018). Gating plots for all samples from each donor were generated with the ggCyto R package (Van et al. 2018), and gates were further reviewed for consistency and batch effects across longitudinal timepoints. For each population gate, a cutoff of 50 events was also set, below which populations were not reported. Proportions for each cell subtype were calculated by dividing the counts for the gated subpopulation by the total number of CD45+ leukocytes for each sample. Proportions of activated cell populations were calculated by dividing the counts for each positive activation marker population by the counts of the corresponding parent population. Samples were run in multiple batches with bridging controls and we determined that the proportion of variability due to batch was lower than biological variability across samples (**Fig. S1b**).

Participant-specific linear modeling of binding antibodies, intercept and slope

Linear mixed effects models were used to estimate binding antibody RBD titer, Y_{ij}, as a function of t_{ij}, the jth time since symptom onset for the ith individual, with random effects for intercept and slope and t_{ij} > 30 days for all i, j:

$$Y_{ij} = \beta_{0i} + \beta_{1i} t_{ij} + \epsilon_{ij}$$

where $\beta_{0i} = \beta_0 + b_i$ and $\beta_{1i} = \beta_1 + c_i$ with (b_i, c_i) iid ~ $N_2(0, \Sigma)$, with

$$\Sigma = \left[\sigma_b^2 \; Cov(b,c) \; Cov(b,c) \; \sigma_c^2 \; \right]$$

and σ_b^2 and σ_c^2 are the between-person variation in the intercept and slope of log RBD titer responses respectively, *Cov(b, c)* is the covariance between the intercept and slope, and ϵ_{ij} iid ~ $N(0, \sigma^2)$. The random effects, b_i and c_i, are each assumed to be independent for different individuals and the within-individual errors ϵ_{ij} are assumed to be independent for different *i, j* and to be independent of the random effects. A similar model was fit to the untransformed IgG N indices, which are linear on the original scale. The function lme from the R package nlme was used to fit the models. Individual-level estimates of the intercepts, slopes, day 30 and day 180 were obtained from the models.

scRNA-seq analysis

Data preprocessing: Binary Base Call (BCL) files were demultiplexed using cellranger mkfastq (10x Genomics v3.0.2) to produce FASTQ files for scRNA-seq and HTO barcode libraries. scRNA-seq FASTQ files for each hashed well were aligned to the 10x Genomics GRCh38 reference transcriptome (10x Genomics vGRCh38-3.0.0) using cellranger (10x Genomics v3.1.1) using default settings. HTO barcode FASTQ files were processed using BarCounter (Swanson et al. 2021) to quantify the count of each HTO barcode for each cell barcode. A custom R pipeline, BarcodeTender (to be released at https://github.com/AllenInstitute/BarcodeTender-pipeline), was used to deconstruct gene-by-cell matrices from cellranger outputs and assign cells to their originating donor sample based on HTO counts. For each well, a threshold was determined for each HTO by removing barcodes with low counts, then performing 1 dimensional k-means clustering to group cells into a "high" or "low" group. The minimum count for the "high" group was set as a cutoff, and all cells above that cutoff were considered positive for that HTO barcode. If the mean of the "high" group was not greater than 4-fold of the mean of the "low" group, the minimum cutoff was updated to the mean of the "low" group, and the process was iterated. If a separation could not be established, the cutoff was set to the maximum count, and all cells were considered negative for the HTO barcode. Cutoffs were then used to binarize cell barcodes as positive or negative for each HTO, and the number of positive HTOs was calculated for each cell barcode. Cell barcodes positive for only one HTO barcode were considered "singlets", and any cells with two or more were considered "multiplets". For each well, count matrices generated by cellranger were split to select singlet cell barcodes from each PBMC sample based on HTO barcodes, then cells from each PBMC sample were concatenated into separate matrices for each donor. Throughout the process, metadata tracking the originating Batch and 10x Chromium Chip and Well were retained to enable batch effect analysis. During the splitting and merging process, quality control reports were generated to allow review prior to downstream analysis.

Cell type labeling: We utilized the supervised PCA projection and anchor-based transfer approach implemented in Seurat v4.0.0 to map cells to a reference projection generated using the Weighted Nearest Neighbor (WNN) graph algorithm, as described in (Hao et al. 2020). A CITE-seq dataset from 8 healthy HIV vaccine volunteers during the course of vaccination was used as the reference dataset to label cells. The CITE-seq reference consisted of 228 surface proteins (antibody-derived tags, ADT) and approximately 160k single cells. The reference consisted of three levels of cell label granularity (Levels 1, 2 and 3). We constructed a level 2.5 label structure that consists of all cell type annotations from level 2 except merging the "CD8 TEM_4" and "CD8 TEM_5" from level 2, into a "CD8 TEMRA" label (based on marker gene expression) and replacing the "Tregs" label in level 2, with "Treg naive" and "Treg memory" labels from level 3, thus spanning a complete spectrum of cell type annotations. We assessed the distribution of label transfer scores per cell and retained cells with a label score ≥0.5. Batch variability was lower than biological variation contributed by cell type and participant-specific differences (**Fig. S1d, S1e**).

Differential expression early acute infection visit compared to uninfected controls: The hurdle model implemented in the MAST package (Finak et al. 2015) was used to identify differentially expressed genes

between the early acute infection COVID-19 participants compared to uninfected controls. An age matched comparison between infected and uninfected controls was performed, i.e older (> 40 years) COVID-19 participants versus older uninfected controls and younger (< 40 years) COVID-19 participants versus younger uninfected controls. Genes that were expressed in at least 10% of all cells were considered for downstream analysis. Gene expression was normalized by scaling raw counts by the total number of reads per cell multiplied by a scaling factor of 10,000, then using a $\log_2$ transformation. A hurdle model was fit on the filtered and normalized data, modeling the infection status and adjusting for the batch for every cell type. A likelihood ratio test was then performed to assess if the coefficients are different from zero. The p-values were adjusted for multiple comparisons using the Benjamini and Hochberg (BH) method (Benjamini and Hochberg 1995). Adjusted p-values < 0.05 were considered significant.

Patient-specific longitudinal gene expression changes: Longitudinal changes in gene expression were also identified using the hurdle model implemented in the MAST package. A hurdle model was fit to each COVID-19 participant independently in order to identify patient-specific longitudinal transcriptomic changes. Genes that were expressed in at least 10% of cells per participant were considered for this analysis. The models were fit on the filtered and normalized data, modeling the days since symptom onset as a continuous variable within each cell type and adjusting for the batch only if any timepoints from the same participant were run across multiple batches. A likelihood ratio test was then performed to assess if the coefficients are different from zero. Obtained p-values are adjusted for multiple comparisons using the BH method. Adjusted p-values < 0.05 were considered significant.

Pathway enrichment analysis: Gene Set Enrichment Analysis (GSEA) (Subramanian et al. 2005) was performed among genes that defined early acute infection status and genes that defined longitudinal changes. A custom collection of genesets that included the Hallmark v7.2 genesets, KEGG v7.2 and Reactomev7.2 from the Molecular Signatures Database (MSigDB, v4.0) was used as the pathway database. The "Type III interferon signaling" gene set was manually curated from the Interferome database (Rusinova et al. 2013). Genes were pre-ranked by the decreasing order of their log fold changes or coefficients. The running sum statistics and Normalized Enrichment Scores (NES) were calculated for each comparison. The pathway enrichment p-values were adjusted using the BH method and pathways with p-values < 0.05 were considered significantly enriched.

Sample-level enrichment (SLEA): Sample-level enrichment analysis (SLEA, Gundem and Lopez-Bigas 2012) was used to represent the GSEA pathway expression results on a per-sample basis. The SLEA score was calculated by first calculating the mean expression value of genes (averaged across single cells) enriched in a pathway, then comparing it to the mean expression of random sets of genes (averaged across single cells) of the same size for 1,000 permutations per sample. The difference between the observed and expected mean expression values for each pathway was determined as the SLEA pathway score per sample.

scATAC-seq analysis

Data preprocessing: scATAC-seq libraries were processed as described previously (Swanson et al. 2021). In brief, cellranger-atac mkfastq (10x Genomics v1.1.0) was used to demultiplex BCL files to FASTQ. FASTQ files were aligned to the human genome (10x Genomics refdata-cellranger-atac-GRCh38-1.1.0) using cellranger-atac count (10x Genomics v1.1.0) with default settings. Fragment positions were used to quantify reads overlapping a reference peak set (GSE123577_pbmc_peaks.bed.gz from GEO accession GSE123577; (Lareau et al. 2019)) which was converted from hg19 to hg38 using the liftOver package for R (Lawrence et al. 2009), ENCODE reference accessible regions (ENCODE file ID ENCFF503GCK; (Vierstra et al. 2020)), and TSS regions (TSS ±2kb from Ensembl v93; (Yates et al. 2020)) for each cell barcode using a bedtools (v2.29.1; (Quinlan and Hall 2010)) analytical pipeline.

Quality Control: Custom R scripts were used to remove cells with less than 1,000 uniquely aligned fragments, less than 20% of fragments overlapping reference peak regions, less than 20% of fragments overlappingENCODE TSS regions, and less than 50% of peaks overlapping ENCODE reference regions. The ArchR package (Granja et al. 2021) was used to assess doublets in scATAC data. Doublets were identified using the ScoreDoublets function using a filter ratio of 8, and cells with DoubletEnrichment scores from 0-1.16 were considered "singlets" and retained for further analysis. Samples with particularly high doublet scores across all cells (>70% of cells with DoubletEnrichment scores > 1.5) were not considered for downstream analysis.

Dimensionality reduction and cell type labeling: We used the ArchR package to generate a count matrix for the PBMC reference peak set described above (Lareau, et al. 2019 Nat Biotech). Dimensionality reduction was performed using the ArchR addIterativeLSI function (parameters varFeatures = 10000, iterations = 2), and the addClusters function was used to identify clusters in LSI dimensions using the Louvain community detection algorithm. For visualization, UMAP was performed using ArchR's addUMAP function with default settings. The ArchR addGeneIntegrationMatrix function (parameters transferParams = list(dims = 1:10, k.weight = 20) was used to label our scATAC cells using the Seurat level 1 cell types from the Seurat v4.0 PBMC reference dataset (Hao et al. 2020). We observed that Louvain clusters contained cells with mixed level 1 identity assignments from label transfer, and cluster labels were often spread across the UMAP space. In comparison, cell type assignments in UMAP coordinates seemed to cleanly separate cell-type identities. To generate clusters that more closely matched label transfer results, we performed K-means clustering on the UMAP coordinates using a range of number of cluster centers from 3 to 50, and identified a set of K-means clusters that each had > 80% of cells sharing a single cell type identity. Almost all such clusters contained >= 98% cells from a single major cell type class (T Cells, B Cells, NKs, or Monocytes/DCs/other), with the exception of a single cluster with 88% purity. We used K-means clusters that shared cell class identities to subset the data into T Cells, B Cells, NKs, or monocytes/DC/other classes for downstream analyses. For each broad type, we performed dimensionality reduction by Iterative LSI using 500 bp genomic tiles. We then performed a second round of label transfer using the ArchR addGeneIntegrationMatrix function (parameters as described for level 1, above) using the higher resolution level 2.5 cell identities (described for scRNA-seq label transfer, above) from the Seurat PBMC reference dataset.

Peak calling and motif enrichment analysis: For each of the broad types above, we grouped cells within each level 2.5 cell type label by donor, and used the ArchR addGroupCoverages and addReproduciblePeakSets functions to perform *de novo* peak calling to identify putative regulatory regions throughout the genome. We ensured that pseudo-bulk replicates derived from donor and cell type intersections were robust by requiring a minimum of 100 cells per pseudo-bulk replicate, with a minimum of 2 replicates for each group.. After identifying *de novo* peak sets, we annotated transcription factor binding sites (TFBS) in all peaks using the ArchR addArchRAnnotations function (parameter collection = "EncodeTFBS") to label binding sites that have been previously observed in ENCODE datasets. We then used the ArchR addBgdPeaks and addDeviationsMatrix functions (parameter peakAnnotation = "EncodeTFBS") , based on ChromVar (Schep et al. 2017), to generate a measure of increased or decreased binding site accessibility compared to a random GC-matched peakset. Differential TFBS usage was computed using the ArchR getMarkerFeatures function (parameters bias = c("TSSEnrichment", "log10(nFrags)"), testMethod = "wilcoxon") to identify differentially accessible genomic regions, followed by the peakAnnoEnrichment function (parameters peakAnnotation = "EncodeTFBS", cutOff = "FDR <= 0.1") to score differentially enriched TFBS deviations. Longitudinal TFBS usage scores were calculated by taking the mean TFBS deviation Z-score for each TF, participant, and time point among COVID19-positive samples.

Linear regression models of early acute infection

Linear regression models were fit to assess changes in normalized protein expression (NPX) for each protein from Olink, as well as flow cytometry or scRNA-seq cell proportions as a function of infection status using the *lm* function from the package *stats* in R. Subject age and biological sex were used as fixed effects in the model in order to control for these potentially confounding variables. P-values were adjusted using the BH method to control false discovery rate (FDR). Adjusted p-values < 0.05 were considered significant.

Linear mixed-effects models of longitudinal infection

Linear mixed-effects models (LME) were fit to assess the longitudinal changes in the serum proteome, flow cytometry and scRNA based cell type proportions as a function of days since symptom onset using the *lme* function (lme4 v1.1-26) implemented in R. Individual NPX protein expression and cell type proportion values were treated as dependent variables. However, COVID-19 patients appear to vary in the slopes and intercepts of days since symptoms. Thus, random effects for both the slope (days since symptom onset) and intercept (participant ID), and fixed effects for age and sex were used in the mixed effects model. P-values were calculated using Wald chi-square tests and adjusted using the BH method to control FDR. Adjusted p-values < 0.05 were considered significant.

Pathways enriched among significant longitudinally changing proteins were identified using Fisher's over-representation analysis. Pathway p-values were adjusted for multiple comparisons using the BH method and pathways significant at adjusted p-value < 0.05 were reported

Outlier analysis

We performed outlier analysis to identify differential proteins in each COVID19 participant. To identify outliers, we calculated mean expression and standard deviation (SD) of each protein in uninfected participants. The normalized protein expression in COVID-19 participants was compared with the average expression from uninfected participants. Outliers were defined as proteins with expression greater than mean ± 2SD (uninfected participants).

Supervised principal coordinate analysis

Supervised principal coordinate analysis (PCoA) was performed on Olink data using the R function *pcoa* from the ape package (v5.5, Paradis and Schliep, 2019, Bioinformatics). Euclidean distances between proteins that were significantly different between COVID-19 participants at Visit 1 and uninfected controls and proteins that significantly changed over time among COVID-19 participants based on the linear regression models and linear mixed effect models were used to define the distance matrix between samples. The distance of a particular sample to the centroid of uninfected controls was then defined as $d = \sqrt{(x - x_0)^2/{s_x}^2 + (y - y_0)^2/{s_y}^2}$, where x, y are the first and the second principal coordinates of the sample while x_0, y_0, s_x, and s_y are the corresponding mean values and standard deviations of uninfected controls.

Integrative cell-cell network analysis

To identify the cell type specific ligand-receptor pairs significantly enriched in COVID-19 patients we selected scRNA-seq data from healthy donors and COVID patient first visit samples for analysis using the nichnetr package (Browaeys, Saelens, and Saeys 2020). The ligand-target model retrieved from the nichnetr package includes 688 ligands and 25,345 potential downstream target genes, with values denoting the prior potential that a particular ligand might regulate the expression of a specific target gene. Receivers and senders were

identified per cell type for plasmablasts, proliferating CD4 T cells, proliferating CD8 T cells, CD14 monocytes, CD16 monocytes, NK cells, proliferating NK cells, cDC1, cDC2, and pDC types. Genes were considered for downstream analysis if expressed in at least 10% of the cells from the corresponding cell type. Background gene expression data was obtained from samples of uninfected control subjects. Ligand-receptor scores were ranked based on Pearson correlation coefficients (PCC). The top 50 identified ligands were then used to infer putatively active ligand-target links using the nichenetr get_weighted_ligand_target_links function with default parameters. The top 10 ligands and their targets were used to visualize the cell type-specific interaction network.

To calculate the changes in the ligand-receptor network as a result of COVID-19 infection, we identified differentially expressed genes from 2 comparisons: 1) acute infection (≤15 days PSO) compared to uninfected controls, and 2) all COVID-19 participant samples compared to uninfected controls (adjusted p-value < 0.05). All proteomic features were included for corresponding change in proteomic features.

KEY RESOURCES TABLE:

REAGENT or RESOURCE	SOURCE	IDENTIFIER	
Antibodies (flow cytometry)			
Marker/Fluorophore	Clone/Vendor	Cat#	Panel
Mouse anti-human CD3/BUV395	UCHT1/BD	563546, RRID:AB_2744387	1,4
Mouse anti-human CD45/BUV496	HI30/BD	624283	1,2,3,4
Mouse anti-human CD15/BUV563	W6D3/BD	624284	1,3
Mouse anti-human CD45RA/BUV615	HI100/BD	624297	1
Mouse anti-human CD14/BUV661	MφP9/BD	741684, RRID:AB_2868407	1
Mouse anti-human CD8/BUV737	RPA-T8/BD	624286	1,4
Mouse anti-human CD11c/BUV805	B-ly6/BD	624287	1,3
Mouse anti-human CD25/BV421	M-A251/BD	562442, RRID:AB_11154578	1
Mouse anti-human CD4/BV480	SK3/BD	566104, RRID:AB_2739506	1
Mouse anti-human CD16/BV605	3G8/BD	563172, RRID:AB_2744297	1
Mouse anti-human CD123/BV650	6H6/BioLegend	306020, RRID:AB_2563827	1
Mouse anti-human CD127/BV711	A019D5/BioLegend	351328, RRID:AB_2562908	1,4
Mouse anti-human IgD/BV750	IA6-2/BD	747484, RRID:AB_2868411	1
Mouse anti-human CD304/BV786	U21-1283/BD	743132, RRID:AB_27412	1
Mouse anti-human CD141/BB515	1A4/BD	565084, RRID:AB_2739058	1,3
Mouse anti-human CD11b/PerCP-Cy5.5	M1/70/BD	561114, RRID:AB_2033995	1
Mouse anti-human CD19/BB790	HIB19/BD	624296	1,3
Mouse anti-human CD27/PE	O323/BioLegend	302808, RRID:AB_314300	1,2
Mouse anti-human abTCR/PE-Dazzle594	IP26/BioLegend	306726, RRID:AB_2566599	1
Mouse anti-human CD34/PE-Cy5	581/BD	555823, RRID:AB_396152	1
Mouse anti-human CD197/PE-Cy7	G043H7/BioLegend	353226, RRID:AB_11126145	1,3,4
Mouse anti-human CD38/APC	HB-7/BioLegend	356606, RRID:AB_2561902	1
Mouse anti-human CD56/APC-R700	NCAM16.2/BD	565139, RRID:AB_2744429	1
Mouse anti-human HLA-DR/APC-Cy7	L243/BioLegend	307618, RRID:AB_493586	1
Mouse anti-human CD38/BUV395	HB7/BD	563811, RRID:AB_2744372	2
Mouse anti-human IgM/BUV563	UCH-B1/BD	624284	2
Mouse anti-human CD56/BUV615	NCAM16.2/BD	613001	2,3
Mouse anti-human CD24/BUV661	ML5/BD	624285	2
Mouse anti-human CD319/BUV737	235614/BD	624491	2
Mouse anti-human CD20/BUV805	2H7/BD	612905	2
Mouse anti-human CD269/BV421	19F2/BioLegend	357520, RRID:AB_2687358	2
Mouse anti-human IgD/BV480	IA6-2/BD	566138, RRID:AB_2739536	2
Mouse anti-human CD268/BV605	11C1/BD	624290	2
Mouse anti-human CD71/BV650	L01.1/BD	624280	2
Mouse anti-human CD274/BV711	29E.2A3/BioLegend	329722, RRID:AB_2565764	2
Mouse anti-human CD3/BV750	SK7/BioLegend	344846, RRID:AB_2800923	2
Mouse anti-human HLA-DR/BV786	G46-6/BD	564041, RRID:AB_2738559	2

Mouse anti-human IgA/FITC	IS11-8E10/Miltenyi Biotec	130-113-475, RRID:AB_2726166	2
Mouse anti-human CD14/BB660	MφP9/BD	624295	2,4
Mouse anti-human IgG/PerCP-Cy5.5	M1310G05/BioLegend	410710, RRID:AB_2565788	2
Mouse anti-human CD86/PE-Dazzle594	BU63/BioLegend	374218, RRID:AB_2814337	2
Mouse anti-human CD10/PE-Cy5	HI10a/BioLegend	312206, RRID:AB_314917	2
Mouse anti-human CD21/PE-Cy7	Bu32/BioLegend	354912, RRID:AB_2561577	2
Mouse anti-human CD85j/APC	GHI/75/BioLegend	333720, RRID:AB_2728294	2
Mouse anti-human CD19/APC-R700	HIB19/BD	564977, RRID:AB_2744308	2
Mouse anti-human 40/APC-Cy7	5C3/BioLegend	334324, RRID:AB_10641702	2
Mouse anti-human CD14/BUV395	MφP9/BD	563561, RRID:AB_2744288	3
Mouse anti-human CD304/BUV661	U21-1283/BD	624285	3
Mouse anti-human CD33/BUV737	HIM3-4/BD	624286	3
Mouse anti-human CX3CR1/BV421	2A9-1/BD	565800, RRID:AB_2744471	3
Mouse anti-human HLA-DR/BV480	G46-6/BD	566113, RRID:AB_2739515	3
Mouse anti-human CD192/BV605	K036C2/BioLegend	357214, RRID:AB_2563876	3
Mouse anti-human CD3/BV650	UCHT1/BioLegend	300468, RRID:AB_2629574	3
Mouse anti-human CD11b/BV711	ICRF44/BioLegend	301344, RRID:AB_2563792	3
Mouse anti-human CD40/BV750	5C3/BD	624380	3
Mouse anti-human CD80/BV786	L307.4/BD	564159, RRID:AB_2738631	3
Mouse anti-human CD123/BB660	7G3/BD	624295	3
Mouse anti-human CD172a/PerCP-efluor710	15-414/Thermo Fisher	46-1729-42, RRID:AB_11043409	3
Mouse anti-human CD370/PE	3A4/Clec9a/BD	563488, RRID:AB_2738237	3
Mouse anti-human CD86/PE-CF594	FUN-1/BD	562390, RRID:AB_11154047	3
Mouse anti-human CD16/PE-Cy5	3G8/BioLegend	302009, RRID:AB_314209	3
Mouse anti-human CD274/APC	29E.2A3/BioLegend	329708, RRID:AB_940360	3
Mouse anti-human CD195/APC-R700	2D7/CCR5/BD	624348	3
Mouse anti-human CD1c/APC-Cy7	L161/BioLegend	331519, RRID:AB_10643413	3
Mouse anti-human CD56/BUV563	NCAM16.2/BD	612928	4
Mouse anti-human CD19/BUV615	HIB19/BD	624297	4
Mouse anti-human CD27/BUV661	L128/BD	624285	4
Mouse anti-human CD39/BUV805	Tu66/BD	624287	4
Mouse anti-human CD103/BV421	Ber-ACT8/BioLegend	350214, RRID:AB_2563514	4
Mouse anti-human abTCR/BV480	IP26/BD	624278	4
Mouse anti-human CD223/BV605	11C3C65/BioLegend	369324, RRID:AB_2721541	4
Mouse anti-human CD95/BV650	DX2/BioLegend	305642, RRID:AB_2632622	4
Mouse anti-human CD278/BV750	DX29/BD	624380	4
Mouse anti-human CD45RA/BV786	HI100/BioLegend	304140, RRID:AB_2563816	4
Mouse anti-human CD185/BB515	RF8B2/BD	564624, RRID:AB_2738871	4
Mouse anti-human CD4/BB700	SK3/BD	566392, RRID:AB_2744421	4
Mouse anti-human HLA-DR/BB790	G46-6/BD	624296	4
Mouse anti-human CD279/PE	EH12.2H7/BioLegend	329906, RRID:AB_940483	4

Mouse anti-human TIGIT/PE-Dazzle594	A15153G/BioLegend	372716, RRID:AB_2632931	4
Mouse anti-human CD38/PE-Cy5	HIT2/BD	555461, RRID:AB_395854	4
Mouse anti-human CD69/APC	FN50/BioLegend	310910, RRID:AB_314845	4
Mouse anti-human CD25/APC-R700	2A3/BD	565106, RRID:AB_2744339	4
Mouse anti-human KLRG1/APC-Fire750	SA231A2/BioLegend	367718, RRID:AB_2687392	4
Software and algorithms			
R (Version 4.0.1, 4.0.2)	The R Foundation	https://www.r-project.org/	
BarCounter	(Swanson et al. 2021)	https://github.com/AllenInstitute/BarCounter-release	
flowCore (2.3.2)	(Hahne et al. 2009)	https://github.com/RGLab/flowCore	
flowWorkspace (4.3.5)	Gottardo Lab	https://github.com/RGLab/flowWorkspace	
ncdfFlow (2.37.0)	Gottardo Lab	https://github.com/RGLab/ncdfFLow	
openCyto (2.3.0)	(Finak et al. 2014)	https://github.com/RGLab/openCyto	
ggCyto (1.19.1)	(Van et al. 2018)	https://github.com/RGLab/ggCyto	
CytoML (2.3.1)	(Finak et al. 2018)	https://github.com/RGLab/CytoML	
tidyverse (1.1.2)	(Wickham 2017)	https://www.tidyverse.org	

Panels:

1: PS1 (Survey)

2: PB1 (B cell)

3: PM1 (Myeloid/dendritic cell)

4: PT1 (T cell)

Note:

BD antibodies with a 600000 cat # are custom conjugates.

Lot Number(s):	Gender:	Age:	Race:	# of Vials:	Target Concentration (per Vial):	Post-Processing Concentration (per Vial):	% Viability:
HMN169517	Male	24	Black	330	10 X 10^6	16.2 x 10^6	94.9%

References

Allenspach, E.J., Soveg, F., Finn, L.S., So, L., Gorman, J.A., Rosen, A.B.I., Skoda-Smith, S., Wheeler, M.M., Barrow, K.A., Rich, L.M., et al. (2021). Germline SAMD9L truncation variants trigger global translational repression. J. Exp. Med. *218*.

Arunachalam, P.S., Wimmers, F., Mok, C.K.P., Perera, R.A.P.M., Scott, M., Hagan, T., Sigal, N., Feng, Y., Bristow, L., Tak-Yin Tsang, O., et al. (2020). Systems biological assessment of immunity to mild versus severe COVID-19 infection in humans. Science *369*, 1210–1220.

Bastard, P., Rosen, L.B., Zhang, Q., Michailidis, E., Hoffmann, H.-H., Zhang, Y., Dorgham, K., Philippot, Q., Rosain, J., Béziat, V., et al. (2020). Autoantibodies against type I IFNs in patients with life-threatening COVID-19. Science *370*.

Bernardes, J.P., Mishra, N., Tran, F., Bahmer, T., Best, L., Blase, J.I., Bordoni, D., Franzenburg, J., Geisen, U., Josephs-Spaulding, J., et al. (2020). Longitudinal Multi-omics Analyses Identify Responses of Megakaryocytes, Erythroid Cells, and Plasmablasts as Hallmarks of Severe COVID-19. Immunity *53*, 1296–1314.e9.

Blanco-Melo, D., Nilsson-Payant, B.E., Liu, W.-C., Uhl, S., Hoagland, D., Møller, R., Jordan, T.X., Oishi, K., Panis, M., Sachs, D., et al. (2020). Imbalanced Host Response to SARS-CoV-2 Drives Development of COVID-19. Cell *181*, 1036–1045.e9.

Bosteels, C., Neyt, K., Vanheerswynghels, M., van Helden, M.J., Sichien, D., Debeuf, N., De Prijck, S., Bosteels, V., Vandamme, N., Martens, L., et al. (2020). Inflammatory Type 2 cDCs Acquire Features of cDC1s and Macrophages to Orchestrate Immunity to Respiratory Virus Infection. Immunity *52*, 1039–1056.e9.

Browaeys, R., Saelens, W., and Saeys, Y. (2020). NicheNet: modeling intercellular communication by linking ligands to target genes. Nat. Methods *17*, 159–162.

Browning, J.L. (2008). Inhibition of the lymphotoxin pathway as a therapy for autoimmune disease. Immunol. Rev. *223*, 202–220.

Carvalho, T., Krammer, F., and Iwasaki, A. (2021). The first 12 months of COVID-19: a timeline of immunological insights. Nat. Rev. Immunol. *21*, 245–256.

Channappanavar, R., and Perlman, S. (2020). Age-related susceptibility to coronavirus infections: role of impaired and dysregulated host immunity. J. Clin. Invest. *130*, 6204–6213.

Chen, P., Nirula, A., Heller, B., Gottlieb, R.L., Boscia, J., Morris, J., Huhn, G., Cardona, J., Mocherla, B., Stosor, V., et al. (2021). SARS-CoV-2 Neutralizing Antibody LY-CoV555 in Outpatients with Covid-19. N. Engl. J. Med. *384*, 229–237.

Cohen, K.W., Linderman, S.L., Moodie, Z., Czartoski, J., Lai, L., Mantus, G., Norwood, C., Nyhoff, L.E., Edara, V.V., Floyd, K., et al. (2021). Longitudinal analysis shows durable and broad immune memory after SARS-CoV-2 infection with persisting antibody responses and memory B and T cells. medRxiv.

Consiglio, C.R., Cotugno, N., Sardh, F., Pou, C., Amodio, D., Rodriguez, L., Tan, Z., Zicari, S., Ruggiero, A., Pascucci, G.R., et al. (2020). The Immunology of Multisystem Inflammatory Syndrome in Children with COVID-19. Cell *183*, 968–981.e7.

Dan, J.M., Mateus, J., Kato, Y., Hastie, K.M., Yu, E.D., Faliti, C.E., Grifoni, A., Ramirez, S.I., Haupt, S., Frazier, A., et al. (2020). Immunological memory to SARS-CoV-2 assessed for up to eight months after infection. bioRxiv.

Davis, H.E., Assaf, G.S., McCorkell, L., Wei, H., Low, R.J., Re'em, Y., Redfield, S., Austin, J.P., and Akrami, A. (2020). Characterizing Long COVID in an International Cohort: 7 Months of Symptoms and Their Impact.

medRxiv.

Del Valle, D.M., Kim-Schulze, S., Huang, H.-H., Beckmann, N.D., Nirenberg, S., Wang, B., Lavin, Y., Swartz, T.H., Madduri, D., Stock, A., et al. (2020). An inflammatory cytokine signature predicts COVID-19 severity and survival. Nat. Med. *26*, 1636–1643.

Dennis, A., Wamil, M., Kapur, S., Alberts, J., Badley, A.D., Decker, G.A., Rizza, S.A., Banerjee, R., and Banerjee, A. Multi-organ impairment in low-risk individuals with long COVID.

Evans, R.A., McAuley, H., Harrison, E.M., Shikotra, A., Singapuri, A., Sereno, M., Elneima, O., Docherty, A.B., Lone, N.I., Leavy, O.C., et al. (2021). Physical, cognitive and mental health impacts of COVID-19 following hospitalisation--a multi-centre prospective cohort study. medRxiv.

Fajgenbaum, D.C., and June, C.H. (2020). Cytokine Storm. N. Engl. J. Med. *383*, 2255–2273.

Filbin, M.R., Mehta, A., Schneider, A.M., Kays, K.R., Guess, J.R., Gentili, M., Fenyves, B.G., Charland, N.C., Gonye, A.L.K., Gushterova, I., et al. (2020). Plasma proteomics reveals tissue-specific cell death and mediators of cell-cell interactions in severe COVID-19 patients. bioRxiv.

Finak, Greg, Wenxin Jiang, and Raphael Gottardo. 2018. “CytoML for Cross-Platform Cytometry Data Sharing.” *Cytometry. Part A: The Journal of the International Society for Analytical Cytology* 93 (12): 1189–96.

Finak, Greg, Andrew McDavid, Masanao Yajima, Jingyuan Deng, Vivian Gersuk, Alex K. Shalek, Chloe K. Slichter, et al. 2015. “MAST: A Flexible Statistical Framework for Assessing Transcriptional Changes and Characterizing Heterogeneity in Single-Cell RNA Sequencing Data.” *Genome Biology* 16 (December): 278.

Fischer, M.B., Goerg, S., Shen, L., Prodeus, A.P., Goodnow, C.C., Kelsoe, G., and Carroll, M.C. (1998). Dependence of germinal center B cells on expression of CD21/CD35 for survival. Science *280*, 582–585.

Forero, A., Ozarkar, S., Li, H., Lee, C.H., Hemann, E.A., Nadjsombati, M.S., Hendricks, M.R., So, L., Green, R., Roy, C.N., et al. (2019). Differential Activation of the Transcription Factor IRF1 Underlies the Distinct Immune Responses Elicited by Type I and Type III Interferons. Immunity *51*, 451–464.e6.

Galani, I.-E., Rovina, N., Lampropoulou, V., Triantafyllia, V., Manioudaki, M., Pavlos, E., Koukaki, E., Fragkou, P.C., Panou, V., Rapti, V., et al. (2021). Untuned antiviral immunity in COVID-19 revealed by temporal type I/III interferon patterns and flu comparison. Nat. Immunol. *22*, 32–40.

Gill, M.A., Long, K., Kwon, T., Muniz, L., Mejias, A., Connolly, J., Roy, L., Banchereau, J., and Ramilo, O. (2008). Differential recruitment of dendritic cells and monocytes to respiratory mucosal sites in children with influenza virus or respiratory syncytial virus infection. J. Infect. Dis. *198*, 1667–1676.

Goshua, G., Pine, A.B., Meizlish, M.L., Chang, C.-H., Zhang, H., Bahel, P., Baluha, A., Bar, N., Bona, R.D., Burns, A.J., et al. (2020). Endotheliopathy in COVID-19-associated coagulopathy: evidence from a single-centre, cross-sectional study. The Lancet Haematology *7*, e575–e582.

Granja, Jeffrey M., M. Ryan Corces, Sarah E. Pierce, S. Tansu Bagdatli, Hani Choudhry, Howard Y. Chang, and William J. Greenleaf. 2021. “Author Correction: ArchR Is a Scalable Software Package for Integrative Single-Cell Chromatin Accessibility Analysis.” *Nature Genetics*, March. https://doi.org/10.1038/s41588-021-00850-x.

de Groen, R.A., Groothuismink, Z.M.A., Liu, B.-S., and Boonstra, A. (2015). IFN-λ is able to augment TLR-mediated activation and subsequent function of primary human B cells. J. Leukoc. Biol. *98*, 623–630.

Guan, W.-J., Ni, Z.-Y., Hu, Y., Liang, W.-H., Ou, C.-Q., He, J.-X., Liu, L., Shan, H., Lei, C.-L., Hui, D.S.C., et al. (2020). Clinical Characteristics of Coronavirus Disease 2019 in China. N. Engl. J. Med. *382*, 1708–1720.

Gundem, Gunes, and Nuria Lopez-Bigas. 2012. “Sample-Level Enrichment Analysis Unravels Shared Stress Phenotypes among Multiple Cancer Types.” *Genome Medicine* 4 (3): 28.

Hadjadj, J., Yatim, N., Barnabei, L., Corneau, A., Boussier, J., Smith, N., Péré, H., Charbit, B., Bondet, V., Chenevier-Gobeaux, C., et al. (2020). Impaired type I interferon activity and inflammatory responses in severe COVID-19 patients. Science *369*, 718–724.

Hao, W., Wang, L., and Li, S. (2020a). FKBP5 Regulates RIG-I-Mediated NF-κB Activation and Influenza A Virus Infection. Viruses *12*.

Hao, Y., Hao, S., Andersen-Nissen, E., and Mauck, W.M. (2020b). Integrated analysis of multimodal single-cell data. bioRxiv.

Huang, C., Huang, L., Wang, Y., Li, X., Ren, L., Gu, X., Kang, L., Guo, L., Liu, M., Zhou, X., et al. (2021). 6-month consequences of COVID-19 in patients discharged from hospital: a cohort study. Lancet *397*, 220–232.

Kaneko, N., Kuo, H.-H., Boucau, J., Farmer, J.R., Allard-Chamard, H., Mahajan, V.S., Piechocka-Trocha, A., Lefteri, K., Osborn, M., Bals, J., et al. (2020). Loss of Bcl-6-Expressing T Follicular Helper Cells and Germinal Centers in COVID-19. Cell *183*, 143–157.e13.

Karki, R., Sharma, B.R., Tuladhar, S., Williams, E.P., Zalduondo, L., Samir, P., Zheng, M., Sundaram, B., Banoth, B., Malireddi, R.K.S., et al. (2021). Synergism of TNF-α and IFN-γ Triggers Inflammatory Cell Death, Tissue Damage, and Mortality in SARS-CoV-2 Infection and Cytokine Shock Syndromes. Cell *184*, 149–168.e17.

Kim, J.H., Talbot, H.K., Mishina, M., Zhu, Y., Chen, J., Cao, W., Reber, A.J., Griffin, M.R., Shay, D.K., Spencer, S.M., et al. (2016). High-dose influenza vaccine favors acute plasmablast responses rather than long-term cellular responses. Vaccine *34*, 4594–4601.

Klein, S.L., and Flanagan, K.L. (2016). Sex differences in immune responses. Nat. Rev. Immunol. *16*, 626–638.

Kuri-Cervantes, L., Pampena, M.B., Meng, W., Rosenfeld, A.M., Ittner, C.A.G., Weisman, A.R., Agyekum, R.S., Mathew, D., Baxter, A.E., Vella, L.A., et al. (2020). Comprehensive mapping of immune perturbations associated with severe COVID-19. Sci Immunol *5*.

Lareau, Caleb A., Fabiana M. Duarte, Jennifer G. Chew, Vinay K. Kartha, Zach D. Burkett, Andrew S. Kohlway, Dmitry Pokholok, et al. 2019. “Droplet-Based Combinatorial Indexing for Massive-Scale Single-Cell Chromatin Accessibility.” *Nature Biotechnology*. https://doi.org/10.1038/s41587-019-0147-6.

Lau, A.W.Y., Turner, V.M., Bourne, K., Hermes, J.R., Chan, T.D., and Brink, R. (2021). BAFFR controls early memory B cell responses but is dispensable for germinal center function. J. Exp. Med. *218*.

Liu, C., Martins, A.J., Lau, W.W., Rachmaninoff, N., Chen, J., Imberti, L., Mostaghimi, D., Fink, D.L., Burbelo, P.D., Dobbs, K., et al. (2021). Time-resolved systems immunology reveals a late juncture linked to fatal COVID-19. Cell *0*.

Logue, J.K., Franko, N.M., McCulloch, D.J., McDonald, D., Magedson, A., Wolf, C.R., and Chu, H.Y. (2021). Sequelae in Adults at 6 Months After COVID-19 Infection. JAMA Netw Open *4*, e210830.

Lucas, C., Wong, P., Klein, J., Castro, T.B.R., Silva, J., Sundaram, M., Ellingson, M.K., Mao, T., Oh, J.E., Israelow, B., et al. (2020). Longitudinal analyses reveal immunological misfiring in severe COVID-19. Nature *584*, 463–469.

Lyubchenko, T., Porto, J.D., Cambier, J.C., and Michael Holers, V. (2005). Coligation of the B Cell Receptor

with Complement Receptor Type 2 (CR2/CD21) Using Its Natural Ligand C3dg: Activation without Engagement of an Inhibitory Signaling Pathway. The Journal of Immunology *174*, 3264–3272.

Ma, H., Zeng, W., He, H., Zhao, D., Yang, Y., Jiang, D., Zhou, P., Qi, Y., He, W., Zhao, C., et al. (2020). COVID-19 diagnosis and study of serum SARS-CoV-2 specific IgA, IgM and IgG by chemiluminescence immunoanalysis. MedRXiv.

Manni, M., Gupta, S., Ricker, E., Chinenov, Y., Park, S.H., Shi, M., Pannellini, T., Jessberger, R., Ivashkiv, L.B., and Pernis, A.B. (2018). Regulation of age-associated B cells by IRF5 in systemic autoimmunity. Nat. Immunol. *19*, 407–419.

Marshall, J.C., Murthy, S., Diaz, J., Adhikari, N.K., Angus, D.C., Arabi, Y.M., Baillie, K., Bauer, M., Berry, S., Blackwood, B., et al. (2020). A minimal common outcome measure set for COVID-19 clinical research. Lancet Infect. Dis. *20*, e192–e197.

Mathew, D., Giles, J.R., Baxter, A.E., Oldridge, D.A., Greenplate, A.R., Wu, J.E., Alanio, C., Kuri-Cervantes, L., Pampena, M.B., D'Andrea, K., et al. (2020). Deep immune profiling of COVID-19 patients reveals distinct immunotypes with therapeutic implications. Science *369*.

McElroy, A.K., Akondy, R.S., Davis, C.W., Ellebedy, A.H., Mehta, A.K., Kraft, C.S., Lyon, G.M., Ribner, B.S., Varkey, J., Sidney, J., et al. (2015). Human Ebola virus infection results in substantial immune activation. Proc. Natl. Acad. Sci. U. S. A. *112*, 4719–4724.

Molony, R.D., Nguyen, J.T., Kong, Y., Montgomery, R.R., Shaw, A.C., and Iwasaki, A. (2017). Aging impairs both primary and secondary RIG-I signaling for interferon induction in human monocytes. Sci. Signal. *10*.

Morris, S.B., Schwartz, N.G., Patel, P., Abbo, L., Beauchamps, L., Balan, S., Lee, E.H., Paneth-Pollak, R., Geevarughese, A., Lash, M.K., et al. (2020). Case Series of Multisystem Inflammatory Syndrome in Adults Associated with SARS-CoV-2 Infection - United Kingdom and United States, March-August 2020. MMWR Morb. Mortal. Wkly. Rep. *69*, 1450–1456.

Myall, K.J., Mukherjee, B., Castanheira, A.M., Lam, J.L., Benedetti, G., Mak, S.M., Preston, R., Thillai, M., Dewar, A., Molyneaux, P.L., et al. (2021). Persistent Post–COVID-19 Interstitial Lung Disease. An Observational Study of Corticosteroid Treatment. Annals ATS *18*, 799–806.

Pappas, D.J., Coppola, G., Gabatto, P.A., Gao, F., Geschwind, D.H., Oksenberg, J.R., and Baranzini, S.E. (2009). Longitudinal system-based analysis of transcriptional responses to type I interferons. Physiol. Genomics *38*, 362–371.

Phan, T.G., Grigorova, I., Okada, T., and Cyster, J.G. (2007). Subcapsular encounter and complement-dependent transport of immune complexes by lymph node B cells. Nat. Immunol. *8*, 992–1000.

Pillai, P.S., Molony, R.D., Martinod, K., Dong, H., Pang, I.K., Tal, M.C., Solis, A.G., Bielecki, P., Mohanty, S., Trentalange, M., et al. (2016). Mx1 reveals innate pathways to antiviral resistance and lethal influenza disease. Science *352*, 463–466.

Rao, D.A., Gurish, M.F., Marshall, J.L., Slowikowski, K., Fonseka, C.Y., Liu, Y., Donlin, L.T., Henderson, L.A., Wei, K., Mizoguchi, F., et al. (2017). Pathologically expanded peripheral T helper cell subset drives B cells in rheumatoid arthritis. Nature *542*, 110–114.

Ravichandran, S., Lee, Y., Grubbs, G., Coyle, E.M., Klenow, L., Akasaka, O., Koga, M., Adachi, E., Saito, M., Nakachi, I., et al. (2021). Longitudinal antibody repertoire in "mild" versus "severe" COVID-19 patients reveals immune markers associated with disease severity and resolution. Science Advances *7*, eabf2467.

Ren, X., Wen, W., Fan, X., Hou, W., Su, B., Cai, P., Li, J., Liu, Y., Tang, F., Zhang, F., et al. (2021). COVID-19 immune features revealed by a large-scale single-cell transcriptome atlas. Cell.

Richardson, S., Hirsch, J.S., Narasimhan, M., Crawford, J.M., McGinn, T., Davidson, K.W., the Northwell COVID-19 Research Consortium, Barnaby, D.P., Becker, L.B., Chelico, J.D., et al. (2020). Presenting Characteristics, Comorbidities, and Outcomes Among 5700 Patients Hospitalized With COVID-19 in the New York City Area. JAMA *323*, 2052–2059.

Saheb Sharif-Askari, N., Saheb Sharif-Askari, F., Mdkhana, B., Al Heialy, S., Alsafar, H.S., Hamoudi, R., Hamid, Q., and Halwani, R. (2021). Enhanced expression of immune checkpoint receptors during SARS-CoV-2 viral infection. Mol Ther Methods Clin Dev *20*, 109–121.

Schep, Alicia N., Beijing Wu, Jason D. Buenrostro, and William J. Greenleaf. 2017. "chromVAR: Inferring Transcription-Factor-Associated Accessibility from Single-Cell Epigenomic Data." *Nature Methods* 14 (10): 975–78.

Schulte-Schrepping, J., Reusch, N., Paclik, D., Baßler, K., Schlickeiser, S., Zhang, B., Krämer, B., Krammer, T., Brumhard, S., Bonaguro, L., et al. (2020). Severe COVID-19 Is Marked by a Dysregulated Myeloid Cell Compartment. Cell *182*, 1419–1440.e23.

Schultze, J.L., and Aschenbrenner, A.C. (2021). COVID-19 and the human innate immune system. Cell *184*, 1671–1692.

Sette, A., and Crotty, S. (2021). Adaptive immunity to SARS-CoV-2 and COVID-19. Cell *184*, 861–880.

Shaigany, S., Gnirke, M., Guttmann, A., Chong, H., Meehan, S., Raabe, V., Louie, E., Solitar, B., and Femia, A. (2020). An adult with Kawasaki-like multisystem inflammatory syndrome associated with COVID-19. Lancet *396*, e8–e10.

Sigfrid, L., Drake, T.M., Pauley, E., Jesudason, E.C., Olliaro, P., Lim, W.S., Gillesen, A., Berry, C., Lowe, D.J., McPeake, J., et al. (2021). Long Covid in adults discharged from UK hospitals after Covid-19: A prospective, multicentre cohort study using the ISARIC WHO Clinical Characterisation Protocol. medRxiv.

Soni, C., Perez, O.A., Voss, W.N., Pucella, J.N., Serpas, L., Mehl, J., Ching, K.L., Goike, J., Georgiou, G., Ippolito, G.C., et al. (2020). Plasmacytoid Dendritic Cells and Type I Interferon Promote Extrafollicular B Cell Responses to Extracellular Self-DNA. Immunity *52*, 1022–1038.e7.

Stamatatos, L., Czartoski, J., Wan, Y.-H., Homad, L.J., Rubin, V., Glantz, H., Neradilek, M., Seydoux, E., Jennewein, M.F., MacCamy, A.J., et al. (2021). mRNA vaccination boosts cross-variant neutralizing antibodies elicited by SARS-CoV-2 infection. Science.

Stephenson, E., Reynolds, G., Botting, R.A., Calero-Nieto, F.J., Morgan, M., Tuong, Z.K., Bach, K., Sungnak, W., Worlock, K.B., Yoshida, M., et al. (2021). The cellular immune response to COVID-19 deciphered by single cell multi-omics across three UK centres (medRxiv).

Subramanian, Aravind, Pablo Tamayo, Vamsi K. Mootha, Sayan Mukherjee, Benjamin L. Ebert, Michael A. Gillette, Amanda Paulovich, et al. 2005. "Gene Set Enrichment Analysis: A Knowledge-Based Approach for Interpreting Genome-Wide Expression Profiles." *Proceedings of the National Academy of Sciences of the United States of America* 102 (43): 15545–50.

Sudre, C.H., Murray, B., Varsavsky, T., Graham, M.S., Penfold, R.S., Bowyer, R.C., Pujol, J.C., Klaser, K., Antonelli, M., Canas, L.S., et al. (2021). Attributes and predictors of long COVID. Nat. Med. *27*, 626–631.

Syedbasha, M., Bonfiglio, F., Linnik, J., Stuehler, C., Wüthrich, D., and Egli, A. (2020). Interferon-λ Enhances the Differentiation of Naive B Cells into Plasmablasts via the mTORC1 Pathway. Cell Rep. *33*, 108211.

Takahashi, T., Ellingson, M.K., Wong, P., Israelow, B., Lucas, C., Klein, J., Silva, J., Mao, T., Oh, J.E., Tokuyama, M., et al. (2020). Sex differences in immune responses that underlie COVID-19 disease outcomes. Nature *588*, 315–320.

U S Department, Human Services National Institutes of Health, National Institute of Allergy, and Infectious Diseases, Division of Aids (2017). Division of AIDS (DAIDS) table for grading the severity of adult and pediatric adverse events, corrected version 2.1 (US Department of Health and Human Services, National Institutes of Health …).

Van, Phu, Wenxin Jiang, Raphael Gottardo, and Greg Finak. 2018. “ggCyto: Next Generation Open-Source Visualization Software for Cytometry.” *Bioinformatics* 34 (22): 3951–53.

Vanderheiden, A., Ralfs, P., Chirkova, T., Upadhyay, A.A., Zimmerman, M.G., Bedoya, S., Aoued, H., Tharp, G.M., Pellegrini, K.L., Manfredi, C., et al. (2020). Type I and Type III Interferons Restrict SARS-CoV-2 Infection of Human Airway Epithelial Cultures. J. Virol. *94*.

Vella, L., Giles, J.R., Baxter, A.E., Oldridge, D.A., Diorio, C., Alanio, C., Pampena, M.B., Wu, J.E., Chen, Z., Huang, Y.J., et al. (2020). Deep Immune Profiling of MIS-C demonstrates marked but transient immune activation compared to adult and pediatric COVID-19. medRxiv.

Wang, E.Y., Mao, T., Klein, J., Dai, Y., Huck, J.D., Liu, F., Zheng, N.S., Zhou, T., Israelow, B., Wong, P., et al. (2020). Diverse Functional Autoantibodies in Patients with COVID-19. medRxiv.

Williamson, E.J., Walker, A.J., Bhaskaran, K., Bacon, S., Bates, C., Morton, C.E., Curtis, H.J., Mehrkar, A., Evans, D., Inglesby, P., et al. (2020). OpenSAFELY: factors associated with COVID-19 death in 17 million patients. Nature.

Woodruff, M.C., Ramonell, R.P., Nguyen, D.C., Cashman, K.S., Saini, A.S., Haddad, N.S., Ley, A.M., Kyu, S., Howell, J.C., Ozturk, T., et al. (2020). Extrafollicular B cell responses correlate with neutralizing antibodies and morbidity in COVID-19. Nat. Immunol. *21*, 1506–1516.

Wrammert, J., Onlamoon, N., Akondy, R.S., Perng, G.C., Polsrila, K., Chandele, A., Kwissa, M., Pulendran, B., Wilson, P.C., Wittawatmongkol, O., et al. (2012). Rapid and massive virus-specific plasmablast responses during acute dengue virus infection in humans. J. Virol. *86*, 2911–2918.

Wu, Z., and McGoogan, J.M. (2020). Characteristics of and important lessons from the coronavirus disease 2019 (COVID-19) outbreak in China: summary of a report of 72 314 cases from the Chinese Center for Disease Control and Prevention. JAMA *323*, 1239–1242.

Yamada, T., Sato, S., Sotoyama, Y., Orba, Y., Sawa, H., Yamauchi, H., Sasaki, M., and Takaoka, A. (2021). RIG-I triggers a signaling-abortive anti-SARS-CoV-2 defense in human lung cells. Nat. Immunol.

Zhang, Q., Bastard, P., Liu, Z., Le Pen, J., Moncada-Velez, M., Chen, J., Ogishi, M., Sabli, I.K.D., Hodeib, S., Korol, C., et al. (2020). Inborn errors of type I IFN immunity in patients with life-threatening COVID-19. Science *370*.

Zhang, Y., Meng, J., Zhang, L., Ramkrishnan, S., and Roy, S. (2019). Extracellular Vesicles with Exosome-like Features Transfer TLRs between Dendritic Cells. Immunohorizons *3*, 186–193.

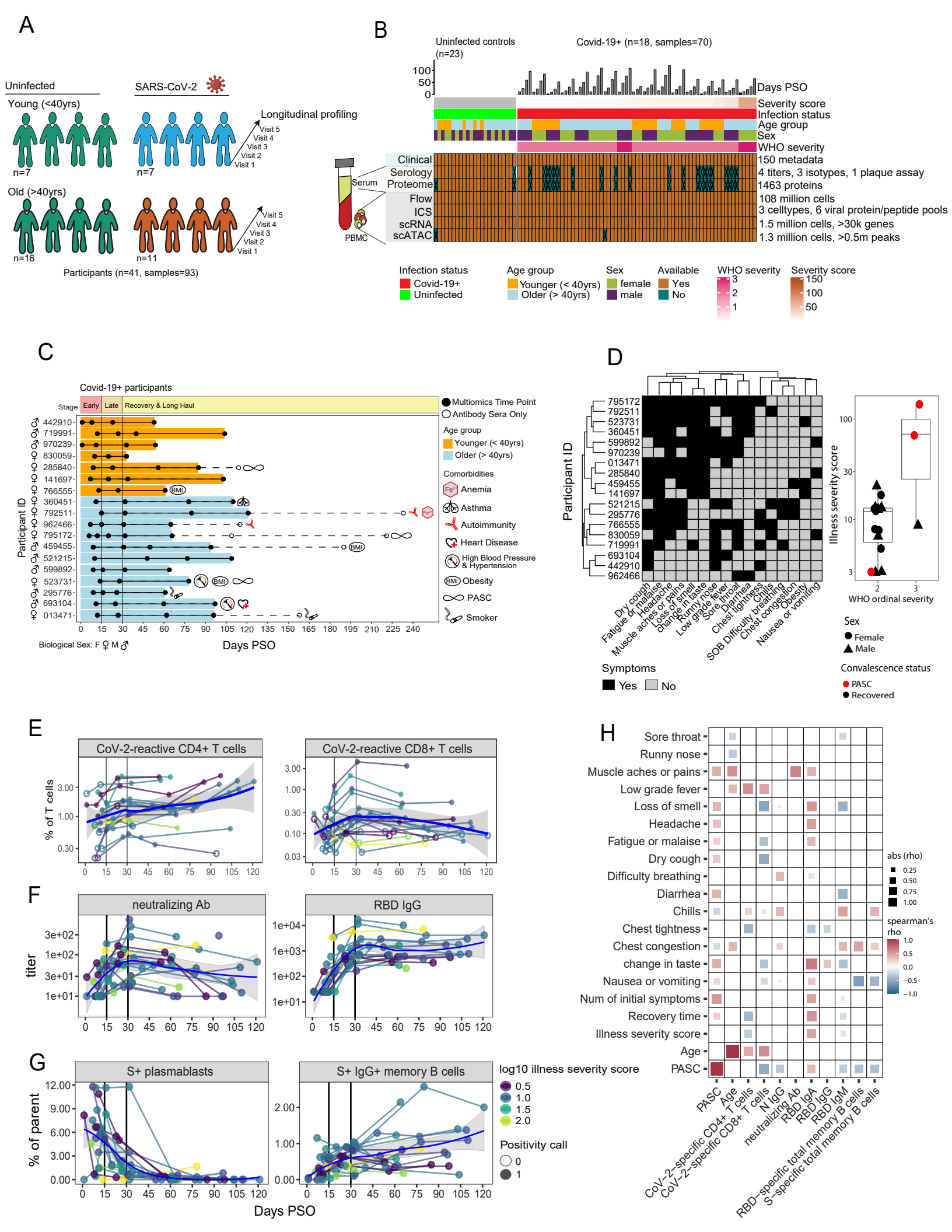
A
Uninfected
SARS-CoV-2
Young (<40yrs)
Longitudinal profiling
Visit 5
Visit 4
Visit 3
Visit 2
Visit 1
n=7
n=7
Old (>40yrs)
n=16
n=11
Participants (n=41, samples=93)
B
Uninfected controls (n=23)
Covid-19+ (n=18, samples=70)
Days PSO
Severity score
Infection status
Age group
Sex
WHO severity
Clinical
Serology
Proteome
Flow
ICS
scRNA
scATAC
Serum
PBMC
150 metadata
4 titers, 3 isotypes, 1 plaque assay
1463 proteins
108 million cells
3 celltypes, 6 viral protein/peptide pools
1.5 million cells, >30k genes
1.3 million cells, >0.5m peaks
Infection status
Covid-19+
Uninfected
Age group
Younger (< 40yrs)
Older (> 40yrs)
Sex
female
male
Available
Yes
No
WHO severity
Severity score
C
Covid-19+ participants
Stage
Early
Late
Recovery & Long Haul
Multiomics Time Point
Antibody Sera Only
Age group
Younger (< 40yrs)
Older (> 40yrs)
Comorbidities
Anemia
Asthma
Autoimmunity
Heart Disease
High Blood Pressure & Hypertension
Obesity
PASC
Smoker
Participant ID
Days PSO
Biological Sex: F ♀ M ♂
D
Participant ID
Illness severity score
WHO ordinal severity
Dry cough
Fatigue or malaise
Headache
Muscle aches or pains
Loss of smell
change in taste
Runny nose
Low grade fever
Sore throat
Diarrhea
Chills
Chest tightness
SOB Difficulty breathing
Chest congestion
Obesity
Nausea or vomiting
Symptoms
Yes
No
Sex
Female
Male
Convalescence status
PASC
Recovered
E
CoV-2-reactive CD4+ T cells
CoV-2-reactive CD8+ T cells
% of T cells
F
neutralizing Ab
RBD IgG
titer
G
S+ plasmablasts
S+ IgG+ memory B cells
% of parent
Days PSO
log10 illness severity score
Positivity call
H
Sore throat
Runny nose
Muscle aches or pains
Low grade fever
Loss of smell
Headache
Fatigue or malaise
Dry cough
Difficulty breathing
Diarrhea
Chills
Chest tightness
Chest congestion
change in taste
Nausea or vomiting
Num of initial symptoms
Recovery time
Illness severity score
Age
PASC
CoV-2-specific CD4+ T cells
CoV-2-specific CD8+ T cells
N IgG
neutralizing Ab
RBD IgA
RBD IgG
RBD IgM
RBD-specific total memory B cells
S-specific total memory B cells
abs (rho)
spearman's rho

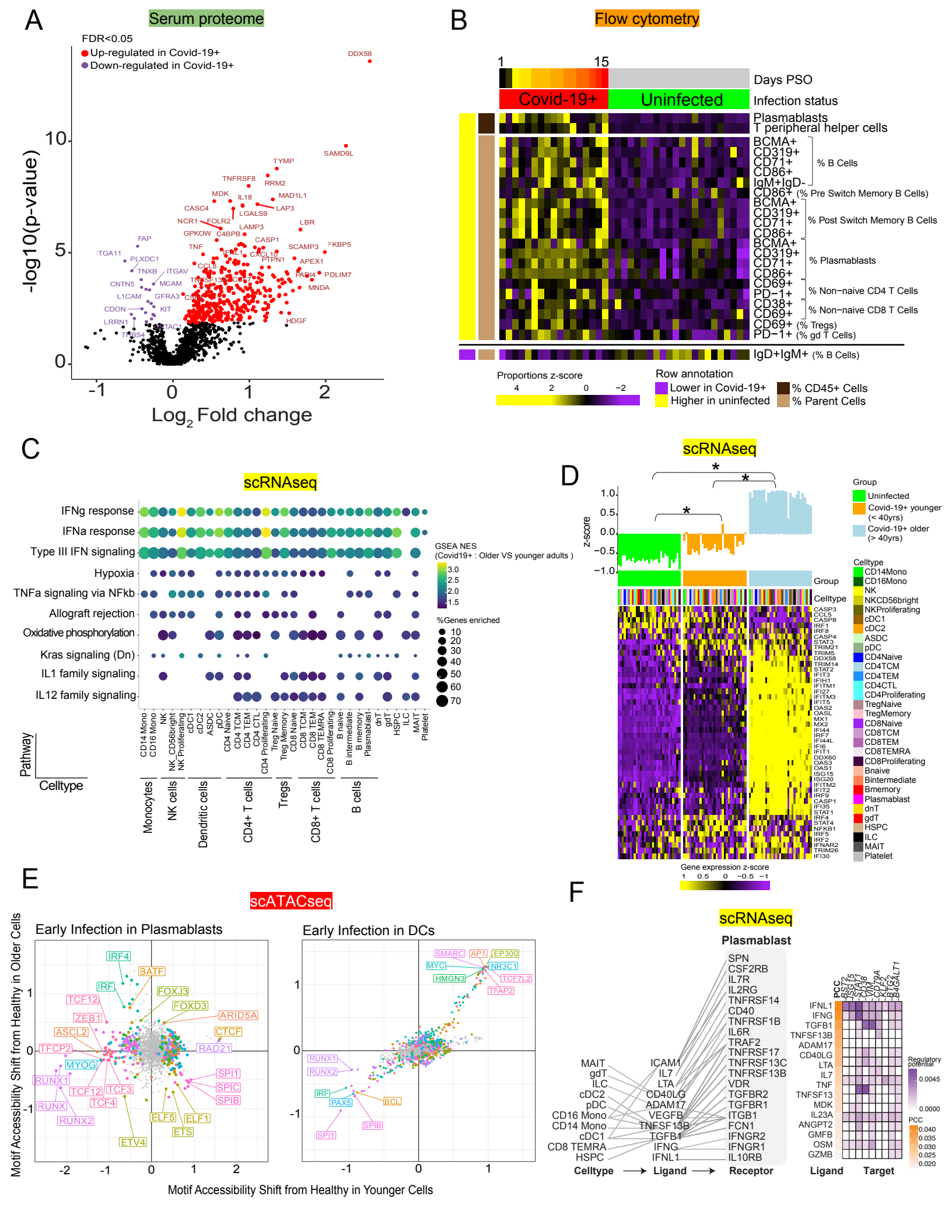
A
Serum proteome
FDR<0.05
Up-regulated in Covid-19+
Down-regulated in Covid-19+
-log10(p-value)
Log2 Fold change
B
Flow cytometry
Days PSO
Infection status
Covid-19+
Uninfected
Plasmablasts
T peripheral helper cells
% B Cells
% Pre Switch Memory B Cells
% Post Switch Memory B Cells
% Plasmablasts
% Non−naive CD4 T Cells
% Non−naive CD8 T Cells
% Tregs
% gd T Cells
% B Cells
Proportions z-score
Row annotation
Lower in Covid-19+
Higher in uninfected
% CD45+ Cells
% Parent Cells
C
scRNAseq
IFNg response
IFNa response
Type III IFN signaling
Hypoxia
TNFa signaling via NFkb
Allograft rejection
Oxidative phosphorylation
Kras signaling (Dn)
IL1 family signaling
IL12 family signaling
GSEA NES
(Covid19+ : Older VS younger adults)
%Genes enriched
Pathway
Celltype
Monocytes
NK cells
Dendritic cells
CD4+ T cells
Tregs
CD8+ T cells
B cells
D
scRNAseq
z-score
Group
Uninfected
Covid-19+ younger (< 40yrs)
Covid-19+ older (> 40yrs)
Celltype
Gene expression z-score
E
scATACseq
Early Infection in Plasmablasts
Early Infection in DCs
Motif Accessibility Shift from Healthy in Older Cells
Motif Accessibility Shift from Healthy in Younger Cells
F
scRNAseq
Plasmablast
Celltype
Ligand
Receptor
Regulatory potential
PCC

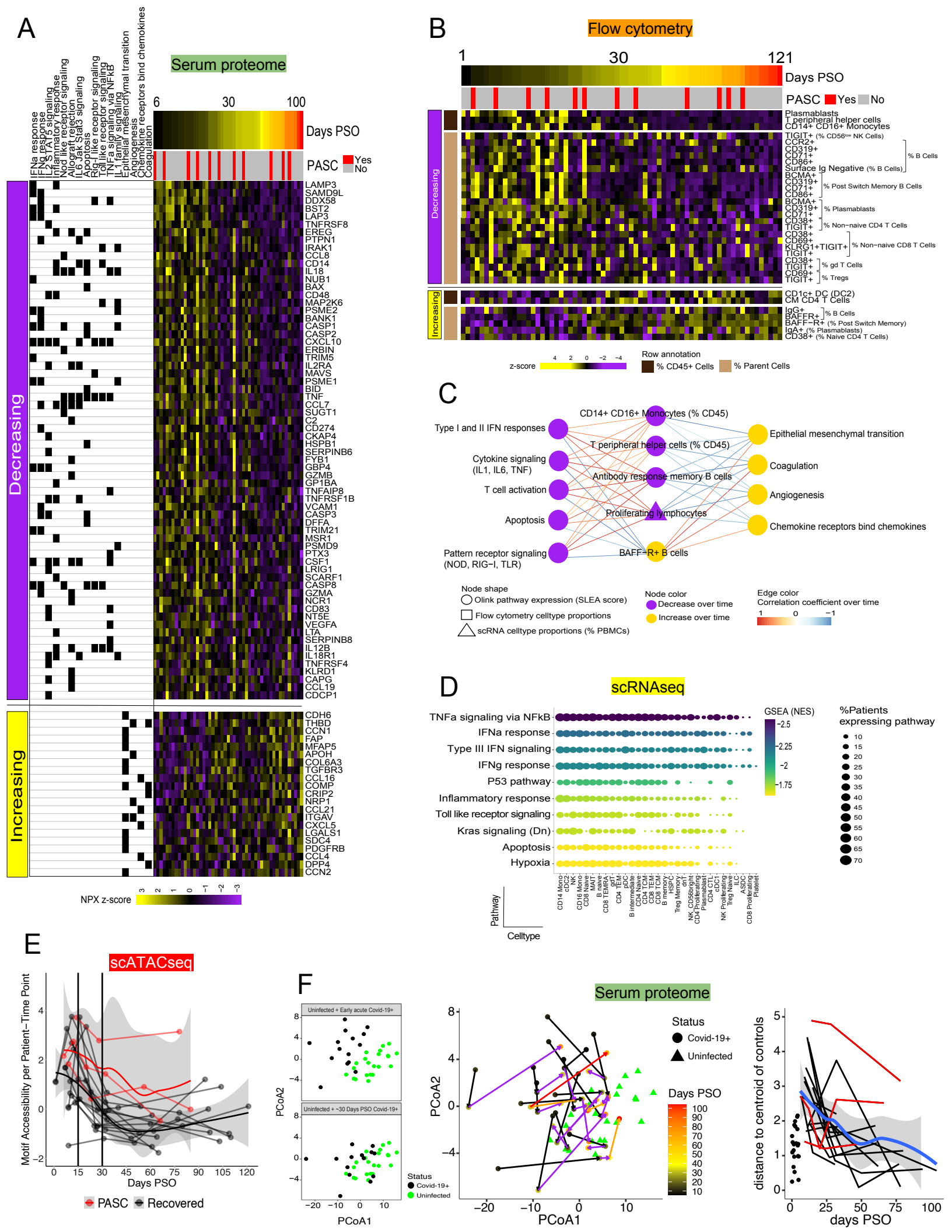
A
Serum proteome
IFNa response
IFNg response
Inflammatory response
Nod like receptor signaling
Allograft rejection
IL6 Jak Stat3 signaling
Apoptosis
Rig-I like receptor signaling
Toll like receptor signaling
TNFa signaling via NFkB
IL1 family signaling
Epithelial mesenchymal transition
Angiogenesis
Chemokine receptors bind chemokines
Coagulation
6
30
100
Days PSO
PASC
Yes
No
Decreasing
Increasing
LAMP3
SAMD9L
DDX58
BST2
LAP3
TNFRSF8
EREG
PTPN1
IRAK1
CCL8
CD14
IL18
NUB1
BAX
CD48
MAP2K6
PSME2
BANK1
CASP1
CASP2
CXCL10
ERBIN
TRIM5
IL2RA
MAVS
PSME1
BID
TNF
CCL7
SUGT1
C2
CD274
CKAP4
HSPB1
SERPINB6
FYB1
GBP4
GZMB
GP1BA
TNFAIP8
TNFRSF1B
VCAM1
CASP3
DFFA
TRIM21
MSR1
PSMD9
PTX3
CSF1
LRIG1
SCARF1
CASP8
GZMA
NCR1
CD83
NT5E
VEGFA
LTA
SERPINB8
IL12B
IL18R1
TNFRSF4
KLRD1
CAPG
CCL19
CDCP1
CDH6
THBD
CCN1
FAP
MFAP5
APOH
COL6A3
TGFBR3
CCL16
COMP
CRIP2
NRP1
CCL21
ITGAV
CXCL5
LGALS1
SDC4
PDGFRB
CCL4
DPP4
CCN2
NPX z-score
3
2
1
0
−1
−2
−3
B
Flow cytometry
1
30
121
Days PSO
PASC
Yes
No
Decreasing
Increasing
Plasmablasts
T peripheral helper cells
CD14+ CD16+ Monocytes
TIGIT+ (% CD56bright NK Cells)
CCR2+
CD319+
CD71+
CD86+
Surface Ig Negative (% B Cells)
% B Cells
BCMA+
CD319+
CD71+
CD86+
% Post Switch Memory B Cells
BCMA+
CD319+
CD71+
% Plasmablasts
CD38+
TIGIT+
% Non−naive CD4 T Cells
CD38+
CD69+
KLRG1+TIGIT+
TIGIT+
% Non−naive CD8 T Cells
CD38+
TIGIT+
% gd T Cells
CD69+
TIGIT+
% Tregs
CD1c+ DC (DC2)
CM CD4 T Cells
IgG+
BAFFR+
% B Cells
BAFF−R+ (% Post Switch Memory)
IgA+ (% Plasmablasts)
CD38+ (% Naive CD4 T Cells)
z-score
4
2
0
−2
−4
Row annotation
% CD45+ Cells
% Parent Cells
C
CD14+ CD16+ Monocytes (% CD45)
Type I and II IFN responses
T peripheral helper cells (% CD45)
Epithelial mesenchymal transition
Cytokine signaling
(IL1, IL6, TNF)
Antibody response memory B cells
Coagulation
T cell activation
Angiogenesis
Proliferating lymphocytes
Apoptosis
Chemokine receptors bind chemokines
Pattern receptor signaling
(NOD, RIG−I, TLR)
BAFF−R+ B cells
Node shape
Olink pathway expression (SLEA score)
Flow cytometry celltype proportions
scRNA celltype proportions (% PBMCs)
Node color
Decrease over time
Increase over time
Edge color
Correlation coefficient over time
1
0
−1
D
scRNAseq
TNFa signaling via NFkB
IFNa response
Type III IFN signaling
IFNg response
P53 pathway
Inflammatory response
Toll like receptor signaling
Kras signaling (Dn)
Apoptosis
Hypoxia
GSEA (NES)
−2.5
−2.25
−2
−1.75
%Patients
expressing pathway
10
15
20
25
30
35
40
45
50
55
60
65
70
CD14 Mono
cDC2
NK
CD16 Mono
CD8 Naive
MAIT
B naive
CD8 TEMRA
γδT
CD4 TEM
pDC
B intermediate
CD4 Naive
CD4 TCM
CD8 TEM
CD8 TCM
B memory
HSPC
Treg Memory
γδT
NK_CD56bright
CD4 Proliferating
Plasmablast
CD4 CTL
cDC1
NK Proliferating
Treg Naive
ASDC
ILC
CD8 Proliferating
Platelet
Pathway
Celltype
E
scATACseq
Motif Accessibility per Patient−Time Point
4
2
0
−2
0
15
30
45
60
75
90
105
120
Days PSO
PASC
Recovered
F
Uninfected + Early acute Covid-19+
Uninfected + ~30 Days PSO Covid-19+
PCoA2
PCoA1
Status
Covid-19+
Uninfected
Serum proteome
PCoA2
PCoA1
Status
Covid-19+
Uninfected
Days PSO
100
90
80
70
60
50
40
30
20
10
distance to centroid of controls
days PSO

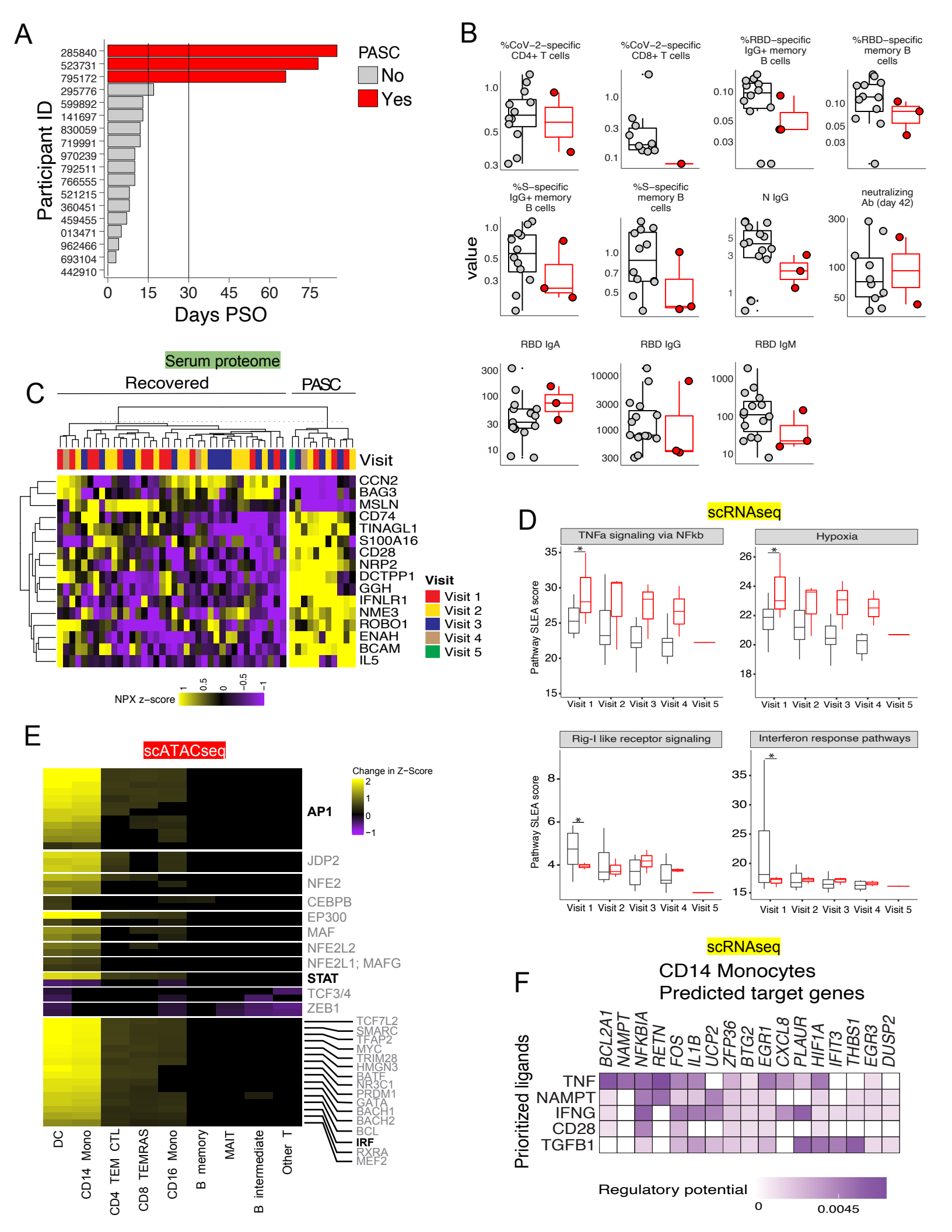
A
Participant ID
285840
523731
795172
295776
599892
141697
830059
719991
970239
792511
766555
521215
360451
459455
013471
962466
693104
442910
0
15
30
45
60
75
Days PSO
PASC
No
Yes
B
%CoV−2−specific CD4+ T cells
%CoV−2−specific CD8+ T cells
%RBD−specific IgG+ memory B cells
%RBD−specific memory B cells
%S−specific IgG+ memory B cells
%S−specific memory B cells
N IgG
neutralizing Ab (day 42)
RBD IgA
RBD IgG
RBD IgM
value
Serum proteome
C
Recovered
PASC
Visit
CCN2
BAG3
MSLN
CD74
TINAGL1
S100A16
CD28
NRP2
DCTPP1
GGH
IFNLR1
NME3
ROBO1
ENAH
BCAM
IL5
Visit
Visit 1
Visit 2
Visit 3
Visit 4
Visit 5
NPX z−score
1
0.5
0
−0.5
−1
D
scRNAseq
TNFa signaling via NFkb
Hypoxia
Rig-I like receptor signaling
Interferon response pathways
Pathway SLEA score
Visit 1
Visit 2
Visit 3
Visit 4
Visit 5
E
scATACseq
Change in Z−Score
AP1
JDP2
NFE2
CEBPB
EP300
MAF
NFE2L2
NFE2L1; MAFG
STAT
TCF3/4
ZEB1
TCF7L2
SMARC
TFAP2
MYC
TRIM28
HMGN3
BATF
NR3C1
PRDM1
GATA
BACH1
BACH2
BCL
IRF
RXRA
MEF2
DC
CD14 Mono
CD4 TEM
CD8 TEMRAS
CD16 Mono
B memory
MAIT
B intermediate
Other T
F
scRNAseq
CD14 Monocytes
Predicted target genes
Prioritized ligands
TNF
NAMPT
IFNG
CD28
TGFB1
BCL2A1
NAMPT
NFKBIA
RETN
FOS
IL1B
UCP2
ZFP36
BTG2
EGR1
CXCL8
PLAUR
HIF1A
IFIT3
THBS1
EGR3
DUSP2
Regulatory potential
0
0.0045

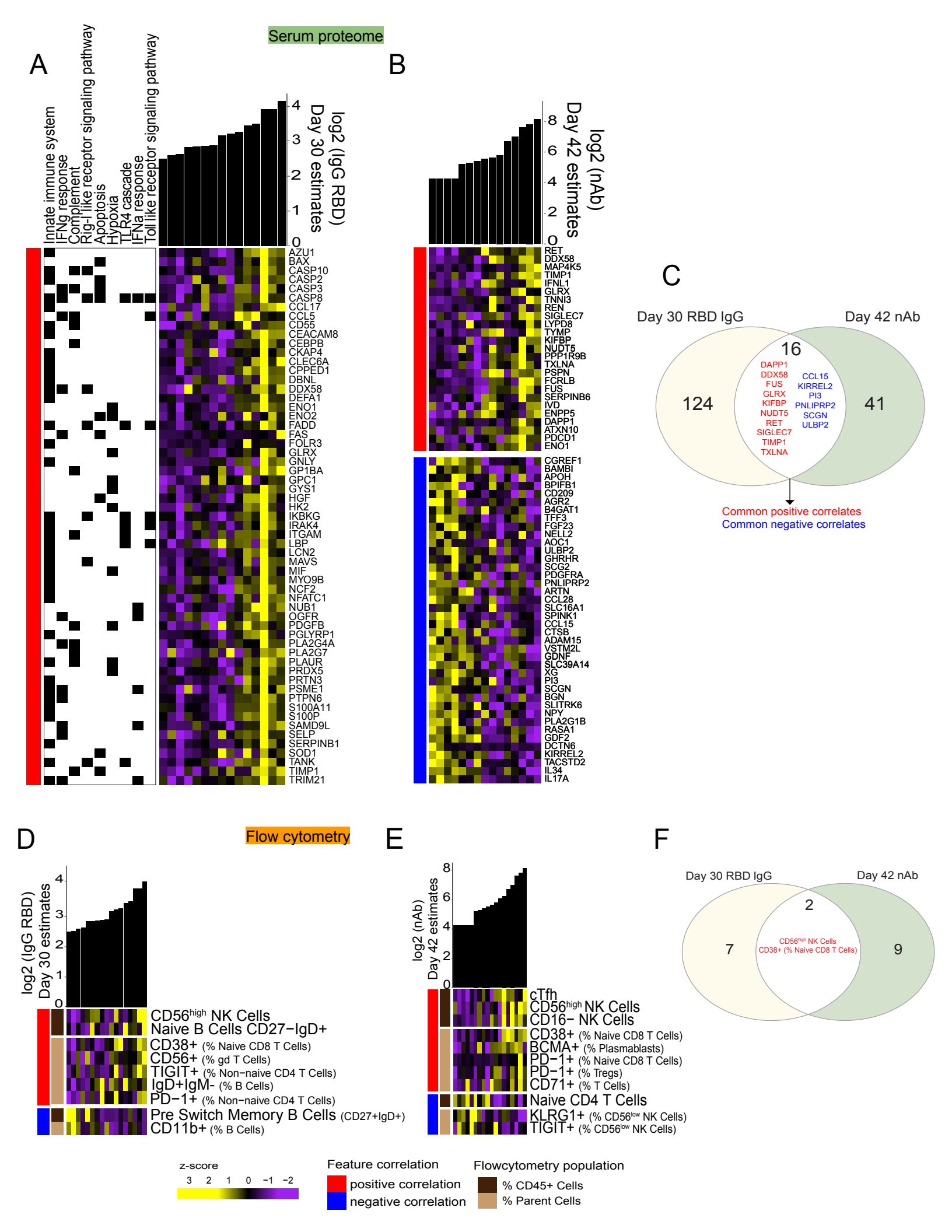
Serum proteome
A
Innate immune system
IFNg response
Complement
Rig-I like receptor signaling pathway
Apoptosis
Hypoxia
TLR4 cascade
IFNa response
Toll like receptor signaling pathway
log2 (IgG RBD)
Day 30 estimates
AZU1
BAX
CASP10
CASP2
CASP3
CASP8
CCL17
CCL5
CD55
CEACAM8
CEBPB
CKAP4
CLEC6A
CPPED1
DBNL
DDX58
DEFA1
ENO1
ENO2
FADD
FAS
FOLR3
GLRX
GNLY
GP1BA
GPC1
GYS1
HGF
HK2
IKBKG
IRAK4
ITGAM
LBP
LCN2
MAVS
MIF
MYO9B
NCF2
NFATC1
NUB1
OGFR
PDGFB
PGLYRP1
PLA2G4A
PLA2G7
PLAUR
PRDX5
PRTN3
PSME1
PTPN6
S100A11
S100P
SAMD9L
SELP
SERPINB1
SOD1
TANK
TIMP1
TRIM21
B
log2 (nAb)
Day 42 estimates
RET
DDX58
MAP4K5
TIMP1
IFNL1
GLRX
TNNI3
REN
SIGLEC7
LYPD8
TYMP
KIFBP
NUDT5
PPP1R9B
TXLNA
PSPN
FCRLB
FUS
SERPINB6
IVD
ENPP5
DAPP1
ATXN10
PDCD1
ENO1
CGREF1
BAMBI
APOH
BPIFB1
CD209
AGR2
B4GAT1
TFF3
FGF23
NELL2
AOC1
ULBP2
GHRHR
SCG2
PDGFRA
PNLIPRP2
ARTN
CCL28
SLC16A1
SPINK1
CCL15
CTSB
ADAM15
VSTM2L
GDNF
SLC39A14
XG
PI3
SCGN
BGN
SLITRK6
NPY
PLA2G1B
RASA1
GDF2
DCTN6
KIRREL2
TACSTD2
IL34
IL17A
C
Day 30 RBD IgG
Day 42 nAb
124
16
41
DAPP1
DDX58
FUS
GLRX
KIFBP
NUDT5
RET
SIGLEC7
TIMP1
TXLNA
CCL15
KIRREL2
PI3
PNLIPRP2
SCGN
ULBP2
Common positive correlates
Common negative correlates
D
Flow cytometry
log2 (IgG RBD)
Day 30 estimates
CD56high NK Cells
Naive B Cells CD27−IgD+
CD38+ (% Naive CD8 T Cells)
CD56+ (% gd T Cells)
TIGIT+ (% Non−naive CD4 T Cells)
IgD+IgM- (% B Cells)
PD−1+ (% Non−naive CD4 T Cells)
Pre Switch Memory B Cells (CD27+IgD+)
CD11b+ (% B Cells)
E
log2 (nAb)
Day 42 estimates
cTfh
CD56high NK Cells
CD16− NK Cells
CD38+ (% Naive CD8 T Cells)
BCMA+ (% Plasmablasts)
PD−1+ (% Naive CD8 T Cells)
PD−1+ (% Tregs)
CD71+ (% T Cells)
Naive CD4 T Cells
KLRG1+ (% CD56low NK Cells)
TIGIT+ (% CD56low NK Cells)
F
Day 30 RBD IgG
Day 42 nAb
7
2
9
CD56high NK Cells
CD38+ (% Naive CD8 T Cells)
z-score
3 2 1 0 −1 −2
Feature correlation
positive correlation
negative correlation
Flowcytometry population
% CD45+ Cells
% Parent Cells

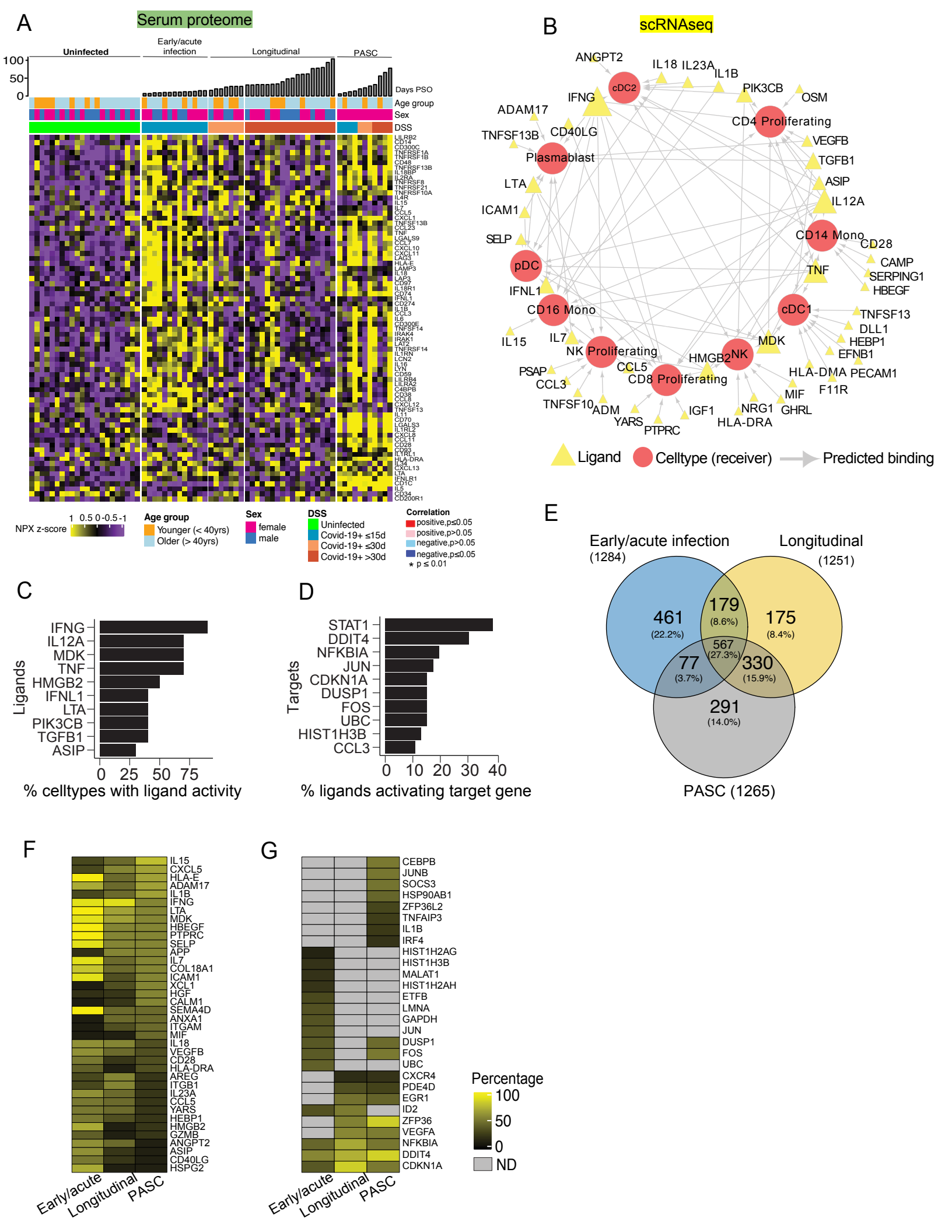
A
Serum proteome
Uninfected
Early/acute infection
Longitudinal
PASC
Days PSO
Age group
Sex
DSS
NPX z-score
Age group
Younger (< 40yrs)
Older (> 40yrs)
Sex
female
male
DSS
Uninfected
Covid-19+ ≤15d
Covid-19+ ≤30d
Covid-19+ >30d
Correlation
positive,p≤0.05
positive,p>0.05
negative,p>0.05
negative,p≤0.05
* p ≤ 0.01
B
scRNAseq
ANGPT2
IL18
IL23A
IL1B
cDC2
IFNG
PIK3CB
OSM
ADAM17
CD4 Proliferating
TNFSF13B
CD40LG
VEGFB
Plasmablast
TGFB1
LTA
ASIP
IL12A
ICAM1
SELP
CD14 Mono
CD28
pDC
CAMP
TNF
SERPING1
IFNL1
HBEGF
CD16 Mono
cDC1
TNFSF13
DLL1
IL15
IL7
MDK
HEBP1
NK Proliferating
HMGB2
NK
EFNB1
PSAP
CCL5
HLA-DMA
PECAM1
CCL3
CD8 Proliferating
F11R
MIF
TNFSF10
ADM
IGF1
NRG1
GHRL
YARS
HLA-DRA
PTPRC
Ligand
Celltype (receiver)
Predicted binding
C
Ligands
IFNG
IL12A
MDK
TNF
HMGB2
IFNL1
LTA
PIK3CB
TGFB1
ASIP
0
25
50
75
% celltypes with ligand activity
D
Targets
STAT1
DDIT4
NFKBIA
JUN
CDKN1A
DUSP1
FOS
UBC
HIST1H3B
CCL3
0
10
20
30
40
% ligands activating target gene
E
Early/acute infection
(1284)
Longitudinal
(1251)
461
(22.2%)
179
(8.6%)
175
(8.4%)
567
(27.3%)
77
(3.7%)
330
(15.9%)
291
(14.0%)
PASC (1265)
F
IL15
CXCL5
HLA-E
ADAM17
IL1B
IFNG
LTA
MDK
HBEGF
PTPRC
SELP
APP
IL7
COL18A1
ICAM1
XCL1
HGF
CALM1
SEMA4D
ANXA1
ITGAM
MIF
IL18
VEGFB
CD28
HLA-DRA
AREG
ITGB1
IL23A
CCL5
YARS
HEBP1
HMGB2
GZMB
ANGPT2
ASIP
CD40LG
HSPG2
Early/acute
Longitudinal
PASC
G
CEBPB
JUNB
SOCS3
HSP90AB1
ZFP36L2
TNFAIP3
IL1B
IRF4
HIST1H2AG
HIST1H3B
MALAT1
HIST1H2AH
ETFB
LMNA
GAPDH
JUN
DUSP1
FOS
UBC
CXCR4
PDE4D
EGR1
ID2
ZFP36
VEGFA
NFKBIA
DDIT4
CDKN1A
Early/acute
Longitudinal
PASC
Percentage
100
50
0
ND